CMS Physics Analysis Summary

Contact: cms-pag-conveners-higgs@cern.ch 2022/03/17

Searches for additional Higgs bosons and vector leptoquarks in $\tau\tau$ final states in proton-proton collisions at $\sqrt{s} = 13$ TeV

The CMS Collaboration

Abstract

Three searches are presented for signatures of physics beyond the standard model (SM) in $\tau\tau$ final states in proton-proton collisions at the CERN LHC, using a data sample collected with the CMS detector at a centre-of-mass energy of $\sqrt{s} = 13$ TeV, corresponding to an integrated luminosity of 138 fb^{-1}. Upper limits at 95% confidence level (CL) are set on the products of the branching fraction for the decay into τ leptons and the cross sections for the production of a resonance ϕ in addition to the observed Higgs boson via gluon fusion (ggϕ) or in association with b quarks, ranging from $\mathcal{O}(10$ pb$)$ (at 60 GeV) to 0.3 fb (at 3.5 TeV) each. The data reveal two excesses for ggϕ production with local p-values equivalent to about three standard deviations at 0.1 and 1.2 TeV. In a search for t-channel exchange of a vector leptoquark U_1, 95% CL upper limits are set on the U_1 coupling to quarks and τ leptons ranging from 1 (at 1 TeV) to 6 (at 5 TeV), depending on the scenario. In the interpretation of minimal supersymmetric SM (MSSM) benchmark scenarios, additional Higgs bosons with masses below 350 GeV are excluded at 95% CL.

This document has been revised with respect to the version dated March 13th, 2022.

1 Introduction

The discovery of a Higgs boson h_{obs} with a mass of 125 GeV at the CERN LHC in 2012 [1–3] has turned the standard model (SM) of particle physics into a theory that could be valid up to the Planck scale. In the SM h_{obs} emerges from the spontaneous breaking of the electroweak $SU(2)_L$ symmetry. While the nature of the underlying mechanism leading to this symmetry breaking and the exact form of the required symmetry-breaking potential are still to be explored, to date all properties of h_{obs} are in good agreement with the expectation for a SM Higgs boson with a mass of 125.38 ± 0.14 GeV [4] within an experimental precision of 5–20% [5–8]. The SM still leaves several fundamental questions related to particle physics unaddressed, among those the presence of dark matter and the observed baryon asymmetry in nature. Many extensions of the SM that address these questions require a more complex structure of the part of the theory that is related to $SU(2)_L$ breaking, often referred to as the Higgs sector. Such models usually predict additional scalar states and/or modified properties of h_{obs} with respect to the SM expectation. Supersymmetry (SUSY) [9, 10] is a prominent example of such a model, which in its minimal extension of the SM—the minimal supersymmetric standard model (MSSM) [11, 12]—predicts three neutral and two charged Higgs bosons.

Searches for additional heavy neutral Higgs bosons in the context of the MSSM were carried out in e^+e^- collisions at LEP [13] and in proton-antiproton collisions at the Tevatron [14–17]. At the LHC such searches have been carried out by the ATLAS and CMS Collaborations in the b quark [18–21], dimuon [22–25], and $\tau\tau$ [22, 26–33] final states. The $\tau\tau$ final state has a leading role in these searches, as the τ lepton has a better experimental accessibility with respect to the b quark final state, while the branching fractions to τ leptons are typically much larger than those to muons due to the larger τ lepton mass.

There are several other examples of extended Higgs sectors which could give appreciable resonant $\tau\tau$ production rates in addition to the known SM processes at the LHC, a summary of which can be found in Ref. [34]. Furthermore, models that include additional coloured states that carry both baryon and lepton quantum numbers—known as leptoquarks [35, 36]—can lead to an enhancement in the nonresonant production rates of $\tau\tau$ pairs with large invariant masses, via the *t*-channel exchange. Searches for resonant and nonresonant $\tau\tau$ signatures are thus complementary in the exploration of physics beyond the SM (BSM) at the LHC. Recent searches for single- and pair-production of third-generation leptoquarks at the LHC can be found in Refs. [37–45].

In this note we present the results of three different searches for both resonant and nonresonant $\tau\tau$ signatures:

i) In a first search, upper limits are presented on the product of the branching fraction for the decay into τ leptons and the cross section for the production of a single narrow bosonic resonance with a width that is assumed to be negligible compared to the experimental resolution in addition to h_{obs}, generally referred to as ϕ throughout the note, via gluon fusion ($gg\phi$) or in association with b quarks ($bb\phi$).

ii) In a second search, upper limits of the coupling g_U of a vector leptoquark U_1 in the nonresonant *t*-channel exchange are presented.

iii) In a third search, exclusion contours in selected benchmark scenarios of the MSSM are given, which rely on the multiresonant signal from three neutral Higgs bosons in the $\tau\tau$ final state, of which one is associated with h_{obs}.

The results are based on the proton-proton (pp) collision data collected during the years 2016–2018, at a centre-of-mass energy of 13 TeV, by the CMS experiment. The data correspond to an integrated luminosity of 138 fb^{-1}. The analysis is performed in four $\tau\tau$ final states: $e\mu$, $e\tau_h$, $\mu\tau_h$, and $\tau_h\tau_h$, where e, μ and τ_h indicate τ decays into electrons, muons, and hadrons, respectively. For this analysis the most significant backgrounds are estimated from data, which includes all SM processes with two genuine τ leptons in the final state, and processes where quark- or gluon-induced jets are misidentified as τ_h (jet $\to \tau_h$).

The note is organized as follows. An overview of the phenomenology of the considered BSM physics scenarios is given in Section 2. In Sections 3 and 4 the CMS detector and the event reconstruction are described. Section 5 summarizes the event selection and categorisation used for the extraction of the signal. The data model and systematic uncertainties are described in Sections 6 and 7. Section 8 contains the results of the analysis. A summary is given in Section 9.

2 Phenomenology

Neutral (pseudo-)scalar bosons ϕ appear in many extensions of the SM. They may have different couplings to the upper and lower components of the $SU(2)_L$ fermion fields (associated with up- and down-type fermions) and gauge bosons. In several models, the ϕ couplings to down-type fermions are enhanced with respect to the expectation for an SM Higgs boson of the same mass, while the couplings to up-type fermions and vector bosons are suppressed. This makes down-type fermion final states, such as $\tau\tau$, particularly interesting for searches for neutral Higgs bosons in addition to h_{obs}. An enhancement in the couplings to down-type fermions also increases the $bb\phi$ production cross section relative to $gg\phi$, which is another characteristic signature of these models and motivates the search for enhanced production cross sections in this production mode with respect to the SM expectation.

In a first interpretation of the data, which is meant to be as model-independent as possible, we search for ϕ production via the $gg\phi$ and $bb\phi$ processes, in addition to h_{obs} in a range of $60 \leq m_\phi \leq 3500$ GeV, where m_ϕ denotes the mass of the hypothesized ϕ. Diagrams for these processes are shown in Fig. 1. In a second, more specific interpretation of the data, we search for nonresonant $\tau\tau$ production in a model with vector leptoquarks. Finally, in a third interpretation of the data, we survey the parameter space of a set of indicative benchmark scenarios of the MSSM, which predict multiresonance signatures, one of which is associated with h_{obs}. The most important characteristics of the vector leptoquark model and the MSSM are described in the following.

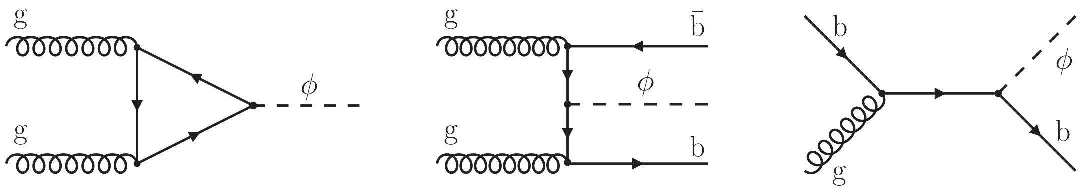

Figure 1: Diagrams for the production of neutral Higgs bosons (left) via gluon fusion ($gg\phi$) and (middle and right) in association with b quarks ($bb\phi$). In the middle panel a pair of b quarks is produced from two gluons. In the right panel ϕ is radiated from a b quark in the proton.

2.1 Vector leptoquarks

Leptoquarks are hypothetical particles that carry both baryon and lepton numbers, and are predicted by several BSM models, such as grand unified theories [46–49], technicolor models [50–

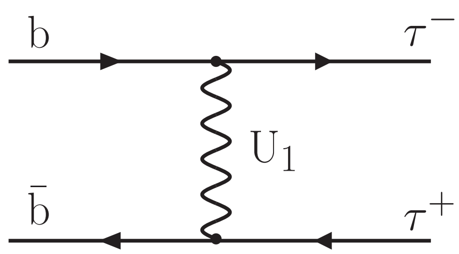

Figure 2: Diagram for the production of a pair of τ leptons via the t-channel exchange of a leptoquark U_1.

53], compositeness scenarios [54, 55], and R-parity violating supersymmetry [9–11, 56–62]. In recent years there has been a renewed interest in leptoquark models as a means of explaining various anomalies observed by a number of B-physics experiments [63–70], most notably the apparent violation of lepton flavour universality in neutral current (NC) [71] and charged current (CC) [72–78] B-meson decays. Models that contain a TeV-scale vector leptoquark (U_1), characterized by its quantum numbers $(SU(3)_C, SU(2)_L, U(1)_Y) = (\mathbf{3}, \mathbf{1}, 2/3)$, are particularly appealing as they can explain both NC and CC anomalies at the same time [64–70].

The Lagrangian for the U_1 coupling to SM fermions is given by [70]

$$\mathcal{L}_U = \frac{g_U}{\sqrt{2}} U^\mu \left[\beta_L^{i\alpha} (\bar{q}_L^i \gamma_\mu l_L^\alpha) + \beta_R^{i\alpha} (\bar{d}_R^i \gamma_\mu e_R^\alpha) \right] + \text{h.c.}, \tag{1}$$

with the coupling constant g_U, where β_L and β_R are left- and right-handed coupling matrices, which are assumed to have the structure:

$$\beta_L = \begin{pmatrix} 0 & 0 & \beta_L^{d\tau} \\ 0 & \beta_L^{s\mu} & \beta_L^{s\tau} \\ 0 & \beta_L^{b\mu} & \beta_L^{b\tau} \end{pmatrix}, \quad \beta_R = \begin{pmatrix} 0 & 0 & 0 \\ 0 & 0 & 0 \\ 0 & 0 & \beta_R^{b\tau} \end{pmatrix}. \tag{2}$$

The normalisation of g_U is chosen to give $\beta_L^{b\tau} = 1$. Two benchmark scenarios are considered, with different assumptions made about the value of $\beta_R^{b\tau}$. In the first benchmark scenario ("VLQ BM 1") $\beta_R^{b\tau}$ is taken to be zero. In the second benchmark scenario ("VLQ BM 2") $\beta_R^{b\tau}$ is taken to be -1, which corresponds to a Pati–Salam-like [47, 66] U_1 leptoquark. The $\beta_L^{s\tau}$ couplings are set to their best fit values from global fits to the low-energy observables presented in Ref. [70], as summarized in Table 1. The $\beta_L^{d\tau}$, $\beta_L^{s\mu}$, and $\beta_L^{b\mu}$ couplings are small and have negligible influence on the $\tau\tau$ signature and therefore have been set to zero.

If the mass of U_1 (m_U) is sufficiently small it will contribute to the $\tau\tau$ spectrum via pair production with each U_1 subsequently decaying to $q\tau$ pairs. For larger m_U the pair production cross section is suppressed by the momentum transfer of the initial state partons in the interaction vertex squared. In this case the dominant contribution to the $\tau\tau$ spectrum is via the t-channel exchange of U_1 in the $b\bar{b}$ initial state as illustrated in Fig. 2, with subdominant contributions from the equivalent $b\bar{s}$, $s\bar{b}$, and $s\bar{s}$ initiated processes. In our analysis we target the kinematic region of $m_U \gtrsim 1$ TeV, motivated by the experimental exclusion limits on m_U by direct searches, e.g. in Ref. [42]. The contribution to the $\tau\tau$ spectrum from U_1 pair production is negligible in this case and we therefore consider only nonresonant production through the t-channel exchange.

Table 1: Summary of the best fit values and uncertainties of $\beta_{L}^{s\tau}$ in the two considered U_1 benchmark scenarios from Ref. [70].

Benchmark	$\beta_{L}^{s\tau}$
VLQ BM 1	$0.19^{+0.06}_{-0.09}$
VLQ BM 2	$0.21^{+0.05}_{-0.09}$

2.2 The MSSM

In the MSSM, which for large scales for the masses of the additional SUSY particles m_{SUSY} turns into a realization of the more general class of effective two Higgs doublet (2HDM) models [79, 80] of type II, the Higgs sector requires two SU(2) doublets, Φ_{u} and Φ_{d}, to provide masses for up- and down-type fermions. In CP-conserving 2HDMs this leads to the prediction of two charged ($H^{\pm}$) and three neutral ϕ bosons (h, H, and A), where h and H (with masses $m_{h} < m_{H}$) are SU(2) scalars, and A is an SU(2) pseudoscalar. The physical states h and H raise as mixtures of the pure gauge fields with a mixing angle α.

At tree level in the MSSM, the masses of these five Higgs bosons, and α, can be expressed in terms of the known gauge boson masses and two additional parameters, which can be chosen as the mass of A (m_{A}) and the ratio of the vacuum expectation values of the neutral components of Φ_{u} and Φ_{d}

$$\tan\beta = \frac{\langle\Phi_{u}^{0}\rangle}{\langle\Phi_{d}^{0}\rangle}. \tag{3}$$

Dependencies on additional parameters of the soft SUSY breaking mechanism enter via higher-order corrections in perturbation theory. In the exploration of the MSSM Higgs sector they are usually set to fixed values in the form of indicative benchmark scenarios to illustrate certain properties of the theory. The most recent set of MSSM benchmark scenarios provided by the LHC Higgs Working Group have been introduced in Refs. [81–83] and summarized in Ref. [84]. The corresponding model input files can be obtained from Ref. [85]. With one exception in these scenarios h takes the role of h_{obs}, and H and A are nearly degenerate in mass ($m_{H} \approx m_{A}$) over a wide spread of the provided parameter space.

At leading-order (LO) in perturbation theory, the coupling of H and A to down-type fermions is enhanced by $\tan\beta$ with respect to the expectation for an SM Higgs boson of the same mass, while the coupling to vector bosons and up-type fermions is suppressed. For increasing values of $\tan\beta$, $bb\phi$ production (with $\phi = H, A$) is enhanced relative to $gg\phi$. The larger contribution of b quarks to the fermion loop in Fig. 1 (left) in addition leads to softer spectra of the H and A transverse momentum (p_{T}). Extra SUSY particles influence the production and decay via higher-order contributions to the interaction vertices that belong to b quark lines. They also contribute directly to the fermion loop in Fig.1 (left).

3 The CMS detector

The central feature of the CMS apparatus is a superconducting solenoid of 6 m internal diameter, providing a magnetic field of 3.8 T. Within the solenoid volume are a silicon pixel and strip tracker, a lead tungstate crystal electromagnetic calorimeter (ECAL), and a brass and scintillator hadron calorimeter, each composed of a barrel and two endcap sections. Forward calorimeters extend the pseudorapidity (η) coverage provided by the barrel and endcap detectors. Muons are measured in gas-ionisation detectors embedded in the steel flux-return yoke outside the solenoid. Events of interest are selected using a two-tiered trigger system. The first level (L1), composed of custom hardware processors, uses information from the calorimeters and muon detectors to select events at a rate of around 100 kHz within a fixed latency of about 4 μs [86]. The second level, known as the high-level trigger (HLT), consists of a farm of processors running a version of the full event reconstruction software optimized for fast processing, and reduces the event rate to around 1 kHz before data storage [87]. A more detailed description of the CMS detector, together with a definition of the coordinate system used and the relevant kinematic variables, can be found in Ref. [88].

4 Event reconstruction

The reconstruction of the pp collision products is based on the particle-flow (PF) algorithm [89], which combines the information from all CMS subdetectors to reconstruct a set of particle candidates, identified as charged and neutral hadrons, electrons, photons, and muons. In the 2016 (2017–2018) data sets the average number of interactions per bunch crossing was 23 (32). The fully recorded detector data of a bunch crossing defines an event for further processing. For each event the candidate vertex with the largest value of summed physics-object p_{T}^{2} is taken to be the primary pp interaction vertex (PV). The physics objects for this purpose are the jets, clustered using the anti-k_{T} jet clustering algorithm as implemented in the FASTJET software package [90] with the tracks assigned to the corresponding candidate vertex as inputs, and the associated missing transverse momentum ($p_{\mathrm{T}}^{\mathrm{miss}}$), taken as the negative vector p_{T} sum of those jets. Secondary vertices, which are detached from the PV, might be associated with decays of long-lived particles emerging from the PV. Any other collision vertices in the event are associated with additional, mostly soft, inelastic pp collisions called pileup (PU).

Electron candidates are reconstructed by fitting tracks in the tracker, and then matching the tracks to clusters in the ECAL [91, 92]. To increase their purity, reconstructed electrons are required to pass a multivariate electron identification discriminant, which combines information on track quality, shower shape, and kinematic quantities. For this analysis, a working point with an identification efficiency of 90% is used, for a rate of jets misidentified as electrons of ≈1%. Muons in the event are reconstructed by performing a simultaneous track fit to hits in the tracker and in the muon detectors [93]. The presence of hits in the muon detectors already leads to a strong suppression of particles misidentified as muons. Additional identification requirements on the track fit quality and the compatibility of individual track segments with the fitted track can reduce the misidentification rate further. For this analysis, muon identification requirements with an efficiency of ≈99% are chosen, with a misidentification rate below 0.2% for pions.

The contributions from backgrounds to the electron and muon selections are further reduced by requiring the corresponding lepton to be isolated from any hadronic activity in the detector. This property is quantified by an isolation variable

$$I_{\mathrm{rel}}^{\mathrm{e}(\mu)} = \frac{1}{p_{\mathrm{T}}^{\mathrm{e}(\mu)}} \left(\sum p_{\mathrm{T}}^{\mathrm{charged}} + \max\left(0, \sum E_{\mathrm{T}}^{\mathrm{neutral}} + \sum E_{\mathrm{T}}^{\gamma} - p_{\mathrm{T}}^{\mathrm{PU}}\right)\right), \quad (4)$$

where $p_{\mathrm{T}}^{\mathrm{e}(\mu)}$ corresponds to the electron (muon) p_{T} and $\sum p_{\mathrm{T}}^{\mathrm{charged}}$, $\sum E_{\mathrm{T}}^{\mathrm{neutral}}$, and $\sum E_{\mathrm{T}}^{\gamma}$ to the p_{T} (transverse energy E_{T}) sum of all charged particles, neutral hadrons, and photons, in a predefined cone of radius $\Delta R = \sqrt{(\Delta\eta)^2 + (\Delta\varphi)^2}$ around the lepton direction at the PV, where $\Delta\eta$ and $\Delta\varphi$ (measured in radians) correspond to the angular distances of the particle to the lepton in the η and azimuthal φ directions. The chosen cone sizes are $\Delta R = 0.3\,(0.4)$ for electrons (muons). The lepton itself is excluded from the calculation. To mitigate any distortions from

Table 2: Selected working points of D_{e}, D_{μ}, and D_{jet} depending on the $\tau\tau$ final state.

	D_{e}	D_{μ}	D_{jet}
$\mathrm{e}\tau_{\mathrm{h}}$	Tight	VLoose	Medium
$\mu\tau_{\mathrm{h}}$	VVloose	Tight	Medium
$\tau_{\mathrm{h}}\tau_{\mathrm{h}}$	VVLoose	VLoose	Medium

PU, only those charged particles whose tracks are associated with the PV are taken into account. Since for neutral hadrons and photons an unambiguous association with the PV or PU is not possible, an estimate of the contribution from PU ($p_{\mathrm{T}}^{\mathrm{PU}}$) is subtracted from the sum of $\sum E_{\mathrm{T}}^{\mathrm{neutral}}$ and $\sum E_{\mathrm{T}}^{\gamma}$. This estimate is obtained from tracks not associated to the PV in the case of I_{rel}^{μ} and from the mean energy flow per area unit in the case of $I_{\mathrm{rel}}^{\mathrm{e}}$. For negative values, the results are set to zero.

For further characterization of the event, all reconstructed PF objects are clustered into jets using the anti-k_{T} jet clustering algorithm with a distance parameter of 0.4. To identify jets resulting from the hadronization of b quarks (b jets) the DEEPJET algorithm is used, as described in Refs. [94, 95]. In this analysis a working point of this algorithm is chosen that corresponds to a b jet identification efficiency of ≈80% for a misidentification rate for jets originating from light quarks or gluons of $\mathcal{O}(1\%)$ [96]. Jets with $p_{\mathrm{T}} > 30\,\mathrm{GeV}$ and $|\eta| < 4.7$ and b jets with $p_{\mathrm{T}} > 20\,\mathrm{GeV}$ and $|\eta| < 2.4\,(2.5)$ are used, where the value in parentheses corresponds to the selection after the upgrade of the silicon pixel detector from 2017 on.

Jets are also used as seeds for the reconstruction of τ_{h} candidates. This is done by exploiting the substructure of the jets, using the "hadrons-plus-strips" algorithm, as described in Refs. [97, 98]. Decays into one or three charged hadrons with up to two neutral pions with $p_{\mathrm{T}} > 2.5\,\mathrm{GeV}$ are used. Neutral pions are reconstructed as strips with dynamic size from reconstructed electrons and photons contained in the seeding jet, where the strip size varies as a function of the p_{T} of the electron or photon candidates. The τ_{h} decay mode is then obtained by combining the charged hadrons with the strips. To distinguish τ_{h} candidates from jets originating from the hadronization of quarks or gluons, and from electrons, or muons, the DEEPTAU (DT) algorithm is used, as described in Ref. [98]. This algorithm exploits the information of the reconstructed event record, comprising tracking, impact parameter, and calorimeter cluster information; the kinematic and object identification properties of the PF candidates in the vicinity of the τ_{h} candidate and the τ_{h} candidate itself; and several characterizing quantities of the whole event. It results in a multiclassification output y_{α}^{DT} ($\alpha = \tau$, e, μ, jet) equivalent to a Bayesian probability of the τ_{h} candidate to originate from a genuine τ lepton, the hadronization of a quark or gluon, an electron, or a muon. From this output three discriminants are built according to

$$D_{\alpha} = \frac{y_{\tau}^{\mathrm{DT}}}{y_{\tau}^{\mathrm{DT}} + y_{\alpha}^{\mathrm{DT}}}, \quad \alpha = \mathrm{e}, \mu, \mathrm{jet}. \tag{5}$$

For the analysis presented here, predefined working points of D_{e}, D_{μ}, and D_{jet} [98] are chosen depending on the $\tau\tau$ final state, as given in Table 2. The VVloose (Tight) working point of D_{e} has an efficiency of 71 (54)% for a misidentification rate of 5.42 (0.05)%. The VLoose (Tight) working point of D_{μ} has an efficiency of 71.1 (70.3)% for a misidentification rate of 0.13 (0.03)%. The Medium working point of D_{jet} has an efficiency 49% for a misidentification rate of 0.43%. It should be noted that the misidentification rate of D_{jet} strongly depends on the p_{T} and quark flavour of the misidentified jet, which is why this number should be viewed as approximate.

The $\vec{p}_{\mathrm{T}}^{\mathrm{miss}}$ is also used for the further categorisation of the events. It is calculated from the negative vector p_{T} sum of all PF candidates, weighted by their probability to originate from the PV [99], exploiting the pileup-per-particle identification algorithm [100] to reduce its PU dependence.

5 Event selection and categorisation

5.1 Selection of $\tau\tau$ candidates

Depending on the final state, the online selection in the HLT step is based either on the presence of a single electron, muon, or τ_h candidate, or an $e\mu$, $e\tau_h$, $\mu\tau_h$, or $\tau_h\tau_h$ pair in the event. In the offline selection further requirements on p_T, η, and $I_{rel}^{e(\mu)}$, are applied in addition to the object identification requirements described in Section 4, as summarized in Table 3.

In the $e\mu$ final state an electron and a muon with $p_T > 15$ GeV and $|\eta| < 2.4$ are required. Depending on the trigger path that has led to the online selection of the event, a stricter requirement of $p_T > 24$ GeV is imposed on one of the two leptons, to ensure a sufficiently high trigger efficiency of the HLT selection. Both leptons are required to be isolated from any hadronic activity in the detector according to $I_{rel}^{e(\mu)} < 0.15\,(0.2)$.

In the $e\tau_h$ ($\mu\tau_h$) final state, an electron (muon) with $p_T > 25\,(20)$ GeV is required, if the event was selected by a trigger based on the presence of the $e\tau_h$ ($\mu\tau_h$) pair in the event. From 2017 onwards, the threshold on the muon is raised to 21 GeV. If the event was selected by a single electron trigger, the p_T requirement on the electron is increased to 26, 28, or 33 GeV for the years 2016, 2017, or 2018, respectively. For muons, the p_T requirement is increased to 23 (25) GeV for 2016 (2017–2018), if selected by a single muon trigger. The electron (muon) is required to be contained in the central detector with $|\eta| < 2.1$, and to be isolated according to $I_{rel}^{e(\mu)} < 0.15$. The τ_h candidate is required to have $|\eta| < 2.3$ and $p_T > 35\,(32)$ GeV if selected by an $e\tau_h$ ($\mu\tau_h$) pair trigger, or $p_T > 30$ GeV if selected by a single electron (muon) trigger. In the $\tau_h\tau_h$ final state, both τ_h candidates are required to have $|\eta| < 2.1$ and $p_T > 40$ GeV. For events only selected by a single τ_h trigger, the τ_h candidate that has been identified with the triggering object is required to have $p_T > 120\,(180)$ GeV for events recorded in 2016 (2017–2018). The chosen working points of the DT discriminants are given in Table 2.

The selected τ decay candidates are required to be of opposite charge and to be separated by more than $\Delta R = 0.3$ in the η–φ plane in the $e\mu$ final state and 0.5 otherwise. The closest distance of their tracks to the PV is required to be $d_z < 0.2$ cm along the beam axis. For electrons and muons, an additional requirement of $d_{xy} < 0.045$ cm in the transverse plane is applied. In rare cases, in which more than one τ_h candidate fulfilling all selection requirements is found, the candidate with the higher D_{jet} score is chosen. For electrons and muons, the most isolated one is chosen.

To avoid the assignment of single events to more than one final state, events with additional electrons or muons, fulfilling looser selection requirements than those given for each corresponding $\tau\tau$ final state above, are rejected from the selection. This requirement also helps with the suppression of background processes, such as Z boson production in the subsequent decay into electrons ($Z \to ee$) or muons ($Z \to \mu\mu$).

5.2 Event categorization

To increase the sensitivity of the searches, all selected events are further split into categories. Events with at least one b jet, according to the selection requirements given in Section 4, are combined into global "b-tag" categories. They are used to target $bb\phi$ production and to con-

Table 3: Offline selection requirements applied to the electron, muon, and τ_h candidates used for the selection of the τ pair. First and second lepton refer to the label of the final state in the first column. For the p_T requirements, the values in parentheses correspond to events that have been recorded based on different trigger paths in the online selection, depending on the data-taking year. A detailed discussion is given in the text.

Final state	First lepton	Second lepton
$e\mu$	$p_T > 15\,(24)$ GeV	$p_T > 24\,(15)$ GeV
	$\lvert\eta\rvert < 2.4$	$\lvert\eta\rvert < 2.4$
	$I_{rel}^{e} < 0.15$	$I_{rel}^{\mu} < 0.2$
$e\tau_h$	$p_T > 25\,(26, 28, 33)$ GeV	$p_T > 35\,(30)$ GeV
	$\lvert\eta\rvert < 2.1$	$\lvert\eta\rvert < 2.3$
	$I_{rel}^{e} < 0.15$	
$\mu\tau_h$	$p_T > 20\,(21, 23, 25)$ GeV	$p_T > 32\,(30)$ GeV
	$\lvert\eta\rvert < 2.1$	$\lvert\eta\rvert < 2.3$
	$I_{rel}^{\mu} < 0.15$	
$\tau_h\tau_h$	$p_T > 40$ GeV	$p_T > 40$ GeV
	$\lvert\eta\rvert < 2.1$	$\lvert\eta\rvert < 2.1$

trol the background from $t\bar{t}$ events. All other events are subsumed into global "no b-tag" categories.

The most discriminating property of a resonant ϕ signal with sufficiently large mass is m_ϕ itself. For smaller masses the distinction of signal by m_ϕ is impeded by the likewise resonant background from $Z/\gamma^* \to \tau\tau$ events. A distinguishing property of the signal compared to this background, gaining importance in this case, is the ϕ transverse momentum.

In the $\tau_h\tau_h$ final state, events are not further categorized. In the $e\mu$, $e\tau_h$, and $\mu\tau_h$ final states, the global categories are further split into two distinct sets of high- ($m_\phi \geq 250$ GeV) and low-mass ($m_\phi < 250$ GeV) categories, as described in the following, where the labels refer to a distinction by the hypothesized value of m_ϕ.

High-mass categories: For $m_\phi \geq 250$ GeV in the $e\tau_h$ ($\mu\tau_h$) final state, more categories are introduced in the global "b-tag" and "no b-tag" categories, based on the transverse mass of the e (μ)-$\vec{p}_T^{\,miss}$ system defined as

$$m_T^{e(\mu)} = m_T(\vec{p}_T^{\,e(\mu)}, \vec{p}_T^{\,miss}), \quad \text{where} \quad m_T(\vec{p}_T^{\,i}, \vec{p}_T^{\,j}) = \sqrt{2\, p_T^i\, p_T^j\, (1 - \cos\Delta\varphi)}, \tag{6}$$

and $\Delta\varphi$ refers to the azimuthal angular difference between $\vec{p}_T^{\,i}$ and $\vec{p}_T^{\,j}$. Events are divided into a Tight- ($m_T^{e(\mu)} < 40$ GeV) and Loose-m_T ($40 \leq m_T^{e(\mu)} < 70$ GeV) category. The ϕ signal is expected to be concentrated in the Tight-m_T category; the Loose-m_T category is kept to increase the signal acceptance for a resonant signal of $m_\phi \gtrsim 700$ GeV.

In the $e\mu$ final state events are categorized based on the observable D_ζ [101] defined as

$$D_\zeta = p_\zeta^{miss} - 0.85\, p_\zeta^{vis}; \qquad p_\zeta^{miss} = \vec{p}_T^{\,miss} \cdot \hat{\zeta}; \qquad p_\zeta^{vis} = \left(\vec{p}_T^{\,e} + \vec{p}_T^{\,\mu}\right) \cdot \hat{\zeta}, \tag{7}$$

where $\hat{\zeta}$ corresponds to the bisectional direction between $\vec{p}_T^{\,e}$ and $\vec{p}_T^{\,\mu}$. The scalar products p_ζ^{miss} and p_ζ^{vis} can take positive or negative values. Their linear combination has been optimized to maximize the sensitivity of the search. For events originating from W boson production in association with jets (W+jets) or $t\bar{t}$ production the $\vec{p}_T^{e}$, $\vec{p}_T^{\mu}$, and $\vec{p}_T^{miss}$ directions are more isotropically distributed leading to nonpeaking distributions in D_ζ. For $\tau\tau$ events from resonant decays, $\vec{p}_T^{miss}$ is expected to roughly coincide with $\hat{\zeta}$, and a stronger correlation between p_ζ^{miss} and p_ζ^{vis} is expected to lead to a peaking distribution about $D_\zeta \approx 0$ GeV.

Three further categories are introduced as High- ($D_\zeta \geq 30$ GeV), Medium- ($-10 \leq D_\zeta < 30$ GeV), and Low-D_ζ ($-35 \leq D_\zeta < -10$ GeV). A resonant signal is expected to be concentrated in the Medium-D_ζ category. However, the Low- and High-D_ζ categories contribute to an increase of the sensitivity of the model-independent ϕ search in the eμ final state by $\approx$10%. A control category in the eμ final state with at least one b jet and $D_\zeta < -35$ GeV is used to constrain the normalization of $t\bar{t}$ events in the statistical analysis used for the extraction of the signal.

In summary, this leads to 17 event categories per data-taking year entering the statistical analysis. In Fig. 3, the D_ζ and m_T^{μ} distributions in the eμ and $\mu\tau_h$ final states are shown, before splitting the events into the high-mass categories. The category definitions are indicated by the vertical dashed lines in the figures. An overview of the high-mass categories is given in Fig. 4.

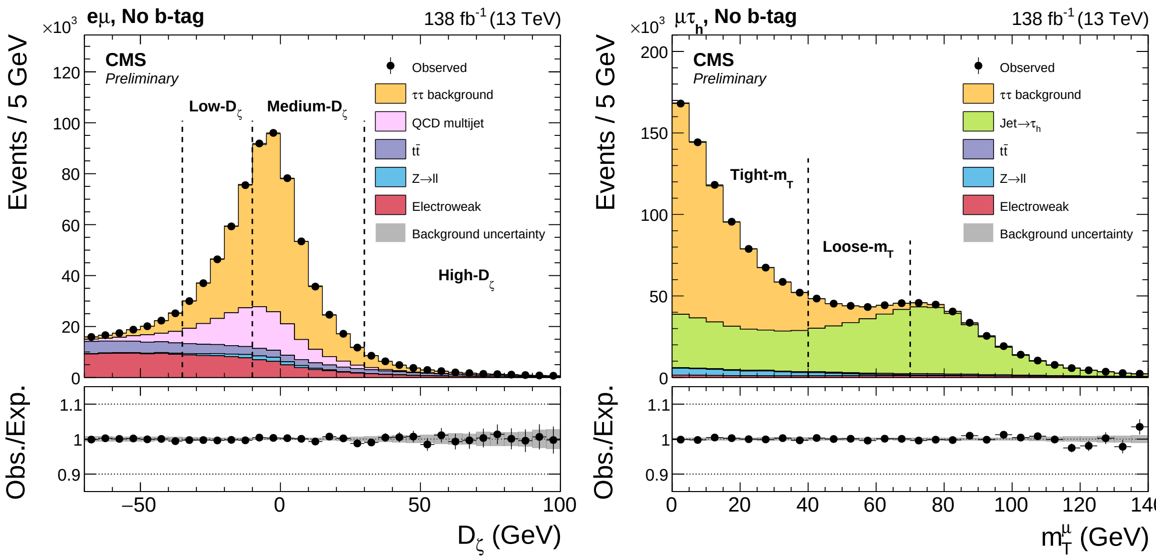

Figure 3: Observed and expected distributions of (left) D_ζ in the eμ final state and (right) m_T^{μ} in the $\mu\tau_h$ final state. The dashed vertical lines indicate the high-mass category definitions in each of the final states. A detailed discussion of the data modelling is given in Section 6. The distributions are shown in the "no b-tag" category before any further event categorization and after a fit to the data in each corresponding variable. The grey shaded band represents the complete set of uncertainties used for signal extraction, after the fit.

Low-mass categories: For $m_\phi < 250$ GeV the high-mass categories are modified in the following way, resulting in the low-mass categories:

i) The Low-D_ζ and Loose-m_T categories, which only improve the signal sensitivity for $m_\phi \gtrsim 700$ GeV are removed.

ii) The remaining "no b-tag categories" are further split by $p_T^{\tau\tau}$, obtained from the vectorial sum p_T of the visible τ decay products and $\vec{p}_T^{miss}$, according to $p_T^{\tau\tau} < 50$ GeV, $50 \leq p_T^{\tau\tau} < 100$ GeV, $100 \leq p_T^{\tau\tau} < 200$ GeV, and $p_T^{\tau\tau} \geq 200$ GeV. No further splitting based on $p_T^{\tau\tau}$ is applied to the "b-tag" categories due to the lower event populations in these categories.

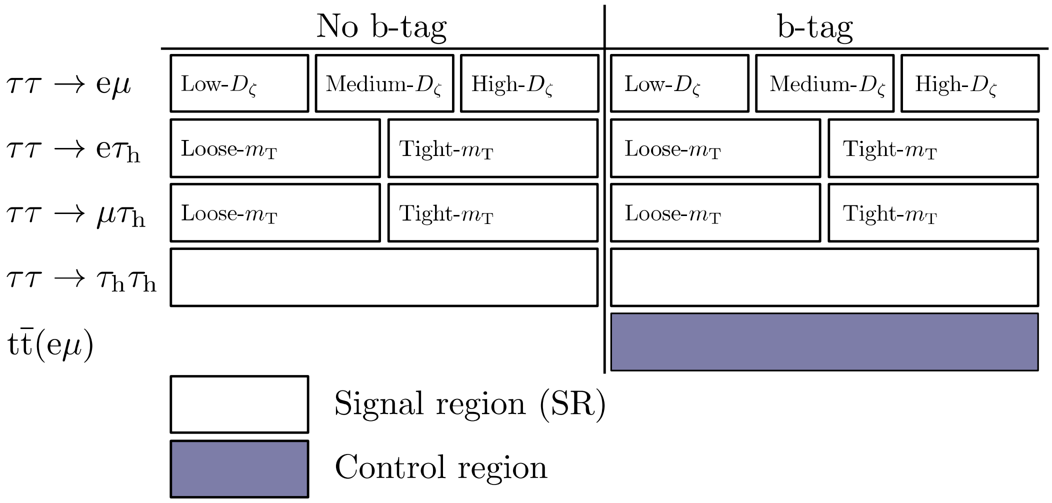

Figure 4: Overview of the high-mass categories used for the extraction of the signal for the model-independent ϕ search for $m_\phi \geq 250\,\text{GeV}$, and the vector leptoquark search and for the interpretation of the data in MSSM benchmark scenarios.

In summary, this leads to 25 event categories per data-taking year entering the statistical analysis. An overview of the low-mass categories is given in Fig. 5.

Use of categories in the analyses: The model-independent ϕ search uses both the high- and low-mass categories for signal extraction; the discriminating variable depends on the category set, as will be discussed in the following. The search for vector leptoquarks and the interpretation of the data in MSSM benchmark scenarios, which both target signals at high mass scales, only make use of the high-mass categories. The interpretation of the data in MSSM benchmark scenarios has the feature that one of the predicted ϕ bosons has to coincide with h_{obs}, with consequences for the signal extraction as discussed in the following.

5.3 Signal extraction

In the low-mass categories the signal is extracted from a likelihood-based estimate of the invariant mass of the $\tau\tau$ system before the decay of the τ leptons [102]. This estimate combines the measurement of $\vec{p}_T^{\,miss}$ and its covariance matrix with the measurements of the visible $\tau\tau$ decay products, utilizing the matrix elements for unpolarized τ decays [103] for the decay into leptons and the two-body phase space [104] for the decay into hadrons. On average the resolution of $m_{\tau\tau}$ amounts to about 15–25% depending on the kinematic properties of the $\tau\tau$ system and the $\tau\tau$ final states, where the latter is related to the number of neutrinos that escape detection.

In the high-mass categories the signal is extracted from distributions of the total transverse mass [26] defined as

$$m_T^{tot} = \sqrt{m_T^2(\vec{p}_T^{\,\tau_1}, \vec{p}_T^{\,\tau_2}) + m_T^2(\vec{p}_T^{\,\tau_1}, \vec{p}_T^{\,miss}) + m_T^2(\vec{p}_T^{\,\tau_2}, \vec{p}_T^{\,miss})}, \tag{8}$$

where $\tau_{1(2)}$ refers to the first (second) τ final state indicated in the $e\mu$, $e\tau_h$, $\mu\tau_h$ and $\tau_h\tau_h$ final state labels, and m_T between two objects with transverse momenta $\vec{p}_T^{\,\tau_1}$ and $\vec{p}_T^{\,\tau_2}$ is defined in Eq. (6).

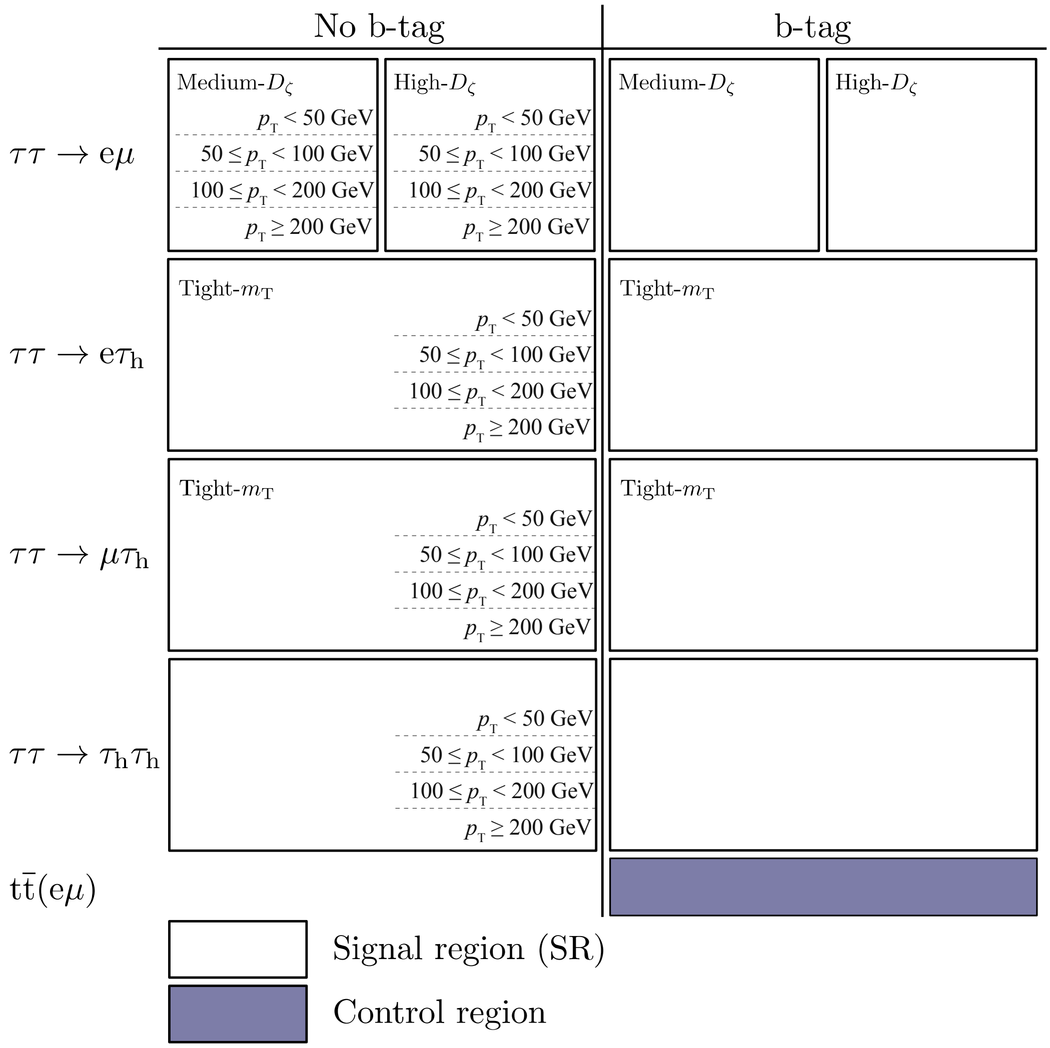

Figure 5: Overview of the low-mass categories used for the extraction of the signal for the model-independent ϕ search for $60 \le m_\phi < 250\,\text{GeV}$.

This is also the case for the search for vector leptoquark t-channel exchange and for the interpretation of the data in MSSM benchmark scenarios. The MSSM predicts three neutral Higgs bosons ϕ, one of which is associated with h_{obs}, and each benchmark scenario that is tested has to match the observed h_{obs} properties. To exploit the best possible experimental knowledge about h_{obs}, in this case, all events in the global "no b-tag" category are split by $m_{\tau\tau}$. For events with $m_{\tau\tau} \ge 250\,\text{GeV}$, the high-mass categories, as described above, are used without change, targeting A and H. For events with $m_{\tau\tau} < 250\,\text{GeV}$, a neural-network (NN) based analysis following a similar strategy as was used for the cross section measurements in Ref. [105] is used to obtain the most precise estimates for h_{obs} production via gluon fusion, vector boson fusion (VBF), and vector boson associated production (Vh), from data.

This modification adds 18 background and 8 signal categories from the NN-analysis per data-taking year. We will refer to these as the "NN-categories" throughout this note. In these categories, the h_{obs} signal is extracted from distributions of the NN output function y_l in each signal and background category. For the NN-analysis in Ref. [105], $m_T^{e\mu}$ calculated from $\vec{p}_T^{\,e} + \vec{p}_T^{\,\mu}$ and

Table 4: Event categories and discriminants used for the extraction of the signals, for the searches described in this note. We note that m_ϕ refers to the hypothesized mass of the model-independent ϕ search, while $m_{\tau\tau}$ refers to the reconstructed mass of the $\tau\tau$ system before the decays of the τ leptons, and thus to an estimate of m_ϕ in data. The variable y_l refers to the output functions of the NNs used for signal extraction [105].

		Signal discrimination	
Search		Low-mass	High-mass
Model-independent (ϕ)	$m_\phi < 250\,\mathrm{GeV}$	$m_{\tau\tau}$	—
	$m_\phi \geq 250\,\mathrm{GeV}$	—	$m_\mathrm{T}^\mathrm{tot}$
Vector leptoquark (U_1)		—	$m_\mathrm{T}^\mathrm{tot}$
MSSM (A, H, h)	$m_{\tau\tau} < 250\,\mathrm{GeV}$	NN output (y_l)	
	$m_{\tau\tau} \geq 250\,\mathrm{GeV}$	—	$m_\mathrm{T}^\mathrm{tot}$

$\vec{p}_\mathrm{T}^\mathrm{miss}$ is required to be less than 60 GeV in the eμ final state, to prevent event overlap with other $\mathrm{h_{obs}}$ decay modes in the SM interpretation. For the analysis presented here, this requirement is replaced by $D_\zeta \geq -35\,\mathrm{GeV}$. An overview of the event categories and discriminants used for signal extraction is given in Table 4.

6 Background and signal modelling

All of the SM background sources that are relevant after the event selection described in Section 5 are listed in Table 5. The expected background composition depends on the $\tau\tau$ final state, event category, and the tested signal mass hypothesis. The most abundant source of background in the b-tag categories is $\mathrm{t\bar{t}}$ production. In the no b-tag categories the decay of Z bosons into τ leptons form the largest fractions of background processes, followed by W+jets production and the events containing purely quantum chromodynamics (QCD) induced gluon and light quark jets, referred to as QCD multijet production. These backgrounds are grouped according to their experimental signature into: (i) events containing genuine τ pairs ($\tau\tau$); (ii) events with quark or gluon induced jets misidentified as τ_h (jet $\to \tau_\mathrm{h}$); (iii) top quark pair events where an intermediate W boson decays into an electron, muon, or τ lepton, and which do not fall into the previous groups (labelled as "$\mathrm{t\bar{t}}$"); (iv) remaining background processes that are of minor importance for the analysis and not yet included in any of the previous event classes (labelled as "misc"); and (v) signal events. Event class (iv) comprises diboson production, single t quark production, Z $\to \mu\mu$, and Z $\to$ ee events.

For the background modelling, four different methods are used depending on the interpreted signature after reconstruction: $\tau\tau$ events are obtained from the τ-embedding method, discussed in Section 6.1; jet $\to \tau_\mathrm{h}$ events are obtained from the "fake factor" (F_F-)method, discussed in Section 6.2; QCD events with eμ pairs in the final state are estimated using the "same sign" (SS-)method, discussed in Section 6.3; all other background events and signal are obtained from full event simulation, discussed in Section 6.4.

6.1 Backgrounds with genuine τ pairs

For all events in which the decay of a Z or two W bosons results in two genuine τ leptons, the τ-embedding method, as described in Ref. [106], is used. For this purpose, $\mu\mu$ events are selected in data. All energy deposits of the muons are removed from the event record and replaced

Table 5: Background processes contributing to the event selection, as given in Section 5. The symbol ℓ corresponds to an electron or muon. The second column refers to the experimental signature in the analysis, the last four columns indicate the estimation methods used to model each corresponding signature, as described in Sections 6.1–6.4.

		Estimation method			
Background process	Final state signature	τ-emb.	F_F	Sim.	SS
	$\tau\tau$	✓	—	—	—
Z	Jet $\to \tau_h$	—	✓	—	—
	$\ell\ell$	—	—	✓	—
	$\tau\tau$	✓	—	—	—
$t\bar{t}$	Jet $\to \tau_h$	—	✓	—	—
	$\ell + X$	—	—	✓	—
	$\tau\tau$	✓	—	—	—
Diboson+single t	Jet $\to \tau_h$	—	✓	—	—
	$\ell + X$	—	—	✓	—
W+jets	Jet $\to \tau_h$	—	✓	—	—
	Jet $\to \ell$	—	—	✓	—
QCD multijet	Jet $\to \tau_h$	—	✓	—	—
	Dijet $\to e\mu$	—	—	—	✓
h	$\tau\tau$	—	—	✓	—

$\ell = e, \mu$

by simulated τ lepton decays with the same kinematic properties as the selected muons. In this way the method relies only on the simulation of the well-understood τ lepton decay and its energy deposits in the detector, while all other parts of the event, like the identification and reconstruction of (b) jets or the non-τ related parts of p_T^{miss} are obtained from data. This results in an improved modelling of the data compared to the simulation of the full process. In turn, several simulation-to-data corrections, as detailed in Section 7.1, are not needed. The selected muons predominantly originate from Z boson decays; however, contributions from other processes resulting in two genuine τ leptons, like $t\bar{t}$ or diboson production, are also covered by this model. A detailed discussion of the selection of the original $\mu\mu$ events, the exact procedure itself, its range of validity, and related uncertainties can be found in Ref. [106]. For a selection with no (at least one) b jet in the event, as described in Section 5, 97% (84%) of the $\mu\mu$ events selected for the τ-embedding method are expected to originate from Z boson decays and <1% (14%) from $t\bar{t}$ production.

6.2 Backgrounds with jets misidentified as hadronic τ decays

The main contributing processes to jet $\to \tau_h$ events are QCD multijet, W+jets, and $t\bar{t}$ production. These events are estimated using the F_F-method, as described in Refs. [32, 107]. For this purpose the complete kinematic phase space is split into the disjoint signal region (SR), application region (AR), and determination regions (DR^i). The SR and the AR differ only in the working point chosen for the identification of the τ_h candidate, where for the AR a looser working point is chosen and the events from the SR are excluded.

For the $\tau_h\tau_h$ final state, either one or both τ_h candidates may originate from jet $\to \tau_h$ misidentification but the dominant process is QCD multijet production, which results in two jet $\to \tau_h$ candidates. In this case, we require only the leading-p_T τ_h to fulfil the AR selection. Consequently, this procedure only provides an estimate for events where the leading τ_h candidate is a misidentified quark- or gluon-initiated jet. The remaining events in which the subleading τ_h candidate is misidentified and the leading τ_h candidate is a genuine τ lepton are modelled via simulation; these events constitute only a small fraction ($\approx$2%) of the total jet $\to \tau_h$ background in this channel.

In the $e\tau_h$ and $\mu\tau_h$ final states, three independent extrapolation factors F_F^i are derived for QCD multijet, W+jets, and $t\bar{t}$ production in three dedicated DR^i, defined to enrich each corresponding process. The F_F^i are then used to estimate the yields N_{SR}^i and kinematic properties of each corresponding background in the SR from the number of events N_{AR}^i in the AR according to

$$N_{SR}^i = F_F^i\, N_{AR}^i \qquad i = \text{QCD, W+jets, } t\bar{t}\,. \tag{9}$$

For the estimate of F_F^{QCD}, we require $0.05 < I_{rel}^{e(\mu)} < 0.15$ and the charges of the two selected ℓ and τ_h candidates to be of same sign. For the estimation of F_F^{W+jets}, the presence of no b jet and $m_T^{e(\mu)} > 70\,\text{GeV}$ are required. The estimation of $F_F^{t\bar{t}}$ is obtained from simulation. Each F_F^i is derived on an event-by-event basis, as a function of the p_T of the τ_h candidate $p_T^{\tau_h}$, the ratio $p_T^{jet}/p_T^{\tau_h}$ where p_T^{jet} is the p_T of the jet seeding the reconstruction of the τ_h candidate, and the jet multiplicity N_{Jets}. Each F_F^i is further subject to a number of bias corrections derived from both control regions in data and simulated event samples to take sub-leading dependencies of the F_F^i into account. Finally, the F_F^i are combined into a weighted sum, using the simulation-based estimation of the fraction w_i of each process in the AR to derive the final factor

$$F_F = \sum_i w_i F_F^i \tag{10}$$

to be used to model this background. In the $\tau_h\tau_h$ final states, F_F^{QCD}, which is by far the dominant process, is used as a proxy for the other processes. For the estimate of F_F^{QCD} in this final state, the charges of the two selected τ_h candidates are required to be of same sign.

6.3 Backgrounds with jets misidentified as electron and muon pairs

The background from QCD multijet production in which two quark- or gluon-induced jets are misidentified as $e\mu$ pairs is estimated using the SS-method. In this case, an AR is distinguished from the SR by requiring the charges of the electron and the muon to have the same sign. A DR is defined requiring $0.2 < I_{rel}^{\mu} < 0.5$ from which a transfer factor F_T is obtained to extrapolate the number N_{AR} of events in the AR to the number N_{SR} of events in the SR according to

$$N_{SR} = F_T\, N_{AR}. \tag{11}$$

The main dependency of F_T is on the distance ΔR (e, μ) between the e and μ trajectories in η–φ, and N_{Jets} being 0, 1, or $\geq$2. Sub-leading dependencies on $\vec{p}_T^{\,e}$, $\vec{p}_T^{\,\mu}$, and the b jet multiplicity $N_{b\text{-jets}}$ are introduced via a bias correction in the DR and a bias correction to account for the fact that F_T has been determined from non-isolated muons. The latter is obtained from another control region with $0.15 < I_{rel}^{e} < 0.5$.

6.4 Simulated backgrounds and signal

In the $\tau_h\tau_h$ final state, the τ-embedding and F_F-methods cover ≈98% of all expected background events. In the $e\tau_h$ and $\mu\tau_h$ final states, the fractions of expected background events described by these two methods are ≈50 and 40%, respectively. In the $e\mu$ final state, ≈53% of all events are covered by either the τ-embedding or SS-methods. All remaining events originate from processes like Z boson, $t\bar{t}$, or diboson production, where at least one decay of a vector boson into an electron or muon is not covered by any of the previously discussed methods. These backgrounds and the signal processes are modelled using the simulation of the full processes.

6.4.1 Background processes

The W+jets and Drell–Yan $Z/\gamma^* \rightarrow \ell\ell$ processes are simulated at LO accuracy in the coupling strength α_S, using the MADGRAPH5_aMC@NLO 2.2.2 (2.4.2) event generator [108, 109] for the simulation of the data taken in 2016 (2017 and 2018). To increase the number of simulated events in regions of high signal purity, supplementary samples are generated with up to four outgoing partons in the hard interaction. For diboson production, MADGRAPH5_aMC@NLO is used at next-to-LO (NLO) precision in α_S. In each case, the FxFx [110] (MLM [111]) prescription is used to match the NLO (LO) matrix element calculation with the parton shower model. For $t\bar{t}$ [112] and single t quark (t-channel) production [113] samples are generated at NLO precision in α_S using POWHEG 2.0 [114–117]. The POWHEG version 1.0 at NLO precision is used for single top quark production in association with a W boson [118].

When compared to data, Z boson, $t\bar{t}$, and single t quark events in the tW channel are normalized to their cross sections at next-to-NLO (NNLO) precision in α_S [119–121]. Single t quark (t-channel) and diboson events are normalized to their cross sections at NLO precision in α_S or higher [121–123].

6.4.2 Signal processes

The kinematic properties of single h production are simulated at NLO precision in α_S using POWHEG 2.0 separately for the production via gluon fusion [124], VBF [125], or in association with a Z (Zh) or W (Wh) boson [126, 127]. For the production via gluon fusion the distributions of the h p_T and the jet multiplicity in the simulation are tuned to match the NNLO accuracy obtained from full phase space calculations with the NNLOPS event generator [128, 129]. For this purpose, h is assumed to behave as expected from the SM. This applies to the modelling of h_{obs} as part of the background for the model-independent ϕ search, as well as for the SM and the MSSM hypotheses for the interpretation of the data in MSSM benchmark scenarios, where h is associated with h_{obs} with properties as expected from the SM.

The gluon fusion signal production of ϕ, H, and A is simulated at NLO precision in α_S using the POWHEG 2.0 implementation for two Higgs doublet models [124]. To account for the multiscale nature of the process in the NLO plus parton shower prediction, the p_T spectra corresponding to the contributions from the t quark alone, the b quark alone, and the tb-interference are each calculated separately. The POWHEG damping factor h_{damp}, which controls the matching between the matrix element calculation and the parton shower, is set specifically for each contribution as suggested in Refs. [130–132].

For the model-independent ϕ search, the individual distributions are combined according to their contribution to the total cross section as expected for an SM Higgs boson with given mass. For the tests of MSSM benchmark scenarios, where the contributions of the individual

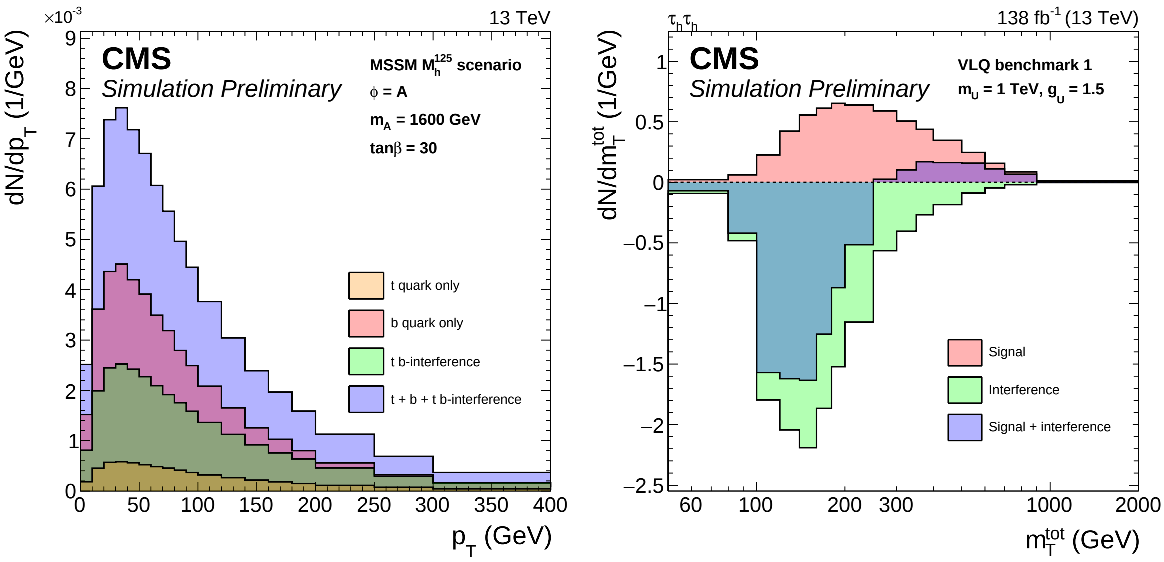

Figure 6: Composition of the differential signal for the MSSM interpretation of the data and the vector leptoquark search. On the left the A p_T density for the MSSM M_h^{125} scenario for $m_A = 1.6$ TeV and $\tan\beta = 30$ is shown, split by the contributions from the t quark only, the b quark only and the tb-interference term. On the right the m_T^{tot} distribution in the $\tau_h\tau_h$ final state, which is the most sensitive final state for the U_1 search, is shown for U_1 t-channel exchange with $m_U = 1$ TeV and $g_U = 1.5$, for the signal with and without the interference term.

distributions also depend on the model parameters, these distributions are scaled using the effective Yukawa couplings as predicted by the corresponding benchmark model [85], before all distributions are combined into one single prediction. In this context, the $\tan\beta$-enhanced SUSY corrections to the Higgs-b quark couplings are also taken into account via the corresponding effective Yukawa coupling, where appropriate. Other SUSY contributions have been checked to amount to less than a few percent and are neglected. An example of the A p_T spectrum for $m_A = 1.6$ TeV and $\tan\beta = 30$ is shown in Fig. 6, left. The production in association with b quarks is simulated at NLO precision in α_S using the corresponding POWHEG 2.0 implementation [133] in the four-flavour scheme (4FS).

The signal process of U_1 t-channel exchange is simulated in the five-flavour scheme (5FS) at LO precision in α_S using the MADGRAPH5_aMC@NLO event generator in the version 2.6.5 [134]. Events are generated with up to one additional outgoing parton from the matrix element calculation and matched following the MLM prescription, with the matching scale Q_{match} set to 40 GeV. The contribution from on-shell $U_1 \to q\tau$ production and decay is excluded during the event generation. Samples are produced with $g_U = 1$, for several values of m_U between 1 and 5 TeV. We observe no large dependence on the assumed U_1 decay width Γ and therefore, for each considered value of m_U, we choose Γ to approximately match the value predicted for U_1 production with couplings as obtained from the global fit of the low-energy observables presented in Ref. [70].

We expect a sizeable effect of destructive interference between the U_1 signal and $Z/\gamma^* \to \tau\tau$ production, where the relative sizes of the interference and non-interference contributions depend on g_U. To take this dependence into account we generate separate samples for each contribution. These are scaled by g_U^4 (for the non-interference contribution) and g_U^2 (for the interference contribution), respectively, to produce the overall signal distributions for any value of g_U. Finally, the signal event yields are normalized to the cross sections computed at LO precision in α_S for the inclusive U_1 mediated $pp \to \tau\tau$ process. The contribution of the U_1 t-channel exchange for $m_{\mathrm{U}} = 1\,\mathrm{TeV}$, $g_{\mathrm{U}} = 1.5$ for the VLQ BM 1 scenario to the $m_{\mathrm{T}}^{\mathrm{tot}}$ distribution in the $\tau_{\mathrm{h}}\tau_{\mathrm{h}}$ final state is shown in Fig. 6, right.

6.4.3 Common processing

The PDF4LHC15 [135] (NNPDF3.1 [136]) parton distribution functions (PDFs) are used for the simulation of the $\mathrm{gg}\phi$ and $\mathrm{bb}\phi$ (U_1) signal processes. For all other processes, the NNPDF3.0 [137] (NNPDF3.1) PDFs are used for the simulation of the data taken in 2016 (2017–2018). The description of the underlying event is parameterized according to the CUETP8M1 [138] and CP5 [139] tunes for the simulation of the data taken in 2016 and 2017–2018, respectively.

Parton showering and hadronization, as well as the τ lepton decays, are modelled using the PYTHIA event generator [140], where versions 8.212 and 8.226 are used for the simulation of the data taken in 2016, and version 8.230 is used for the data taken in 2017–2018. For all simulated events, additional inclusive inelastic pp collisions generated with PYTHIA are added according to the expected PU profile in data to take the effect of the observed PU into account. All events generated are passed through a GEANT4-based [141] simulation of the CMS detector and reconstructed using the same version of the CMS event reconstruction software as used for the data.

7 Systematic uncertainties

The capability of the model to describe the data is monitored in various control regions orthogonal to the signal and background classes, and corrections and corresponding uncertainties are derived where necessary. The corrections and systematic uncertainties are detailed below. The uncertainty model used for the analysis comprises theoretical uncertainties, experimental uncertainties, and uncertainties due to the limited population of template distributions available for the background model. The last group of uncertainties is incorporated for each bin of each corresponding template individually following the approach proposed in Refs. [142, 143]. All other uncertainties lead to correlated changes across bins either in the form of normalization changes or as general nontrivial shape-altering variations. Depending on the way they are derived, correlations may also arise across years, samples, or individual uncertainties.

7.1 Corrections to the model

The following corrections equally apply to simulated and τ-embedded events, where the τ decay is also simulated. Since the simulation part of τ-embedded events happens under detector conditions that are different from the case of fully simulated events, corrections and related uncertainties may differ, as detailed in Ref. [106]. Corrections are derived for residual differences in the efficiency of the selected triggers, differences in the electron and muon tracking efficiency, and in the efficiency of the identification and isolation requirements for electrons and muons. These corrections are obtained in bins of p_{T} and η of the corresponding lepton, using the "tag-and-probe" method, as described in Ref. [144], with $\mathrm{Z} \to \mathrm{ee}$ and $\mathrm{Z} \to \mu\mu$ events. They usually amount to not more than a few percent. The electron energy scale is adjusted to the observation in data using the Z boson mass peak in $\mathrm{Z} \to \mathrm{ee}$ events.

In a similar way, corrections are obtained for the efficiency of triggering on the τ_{h} decay signature and for the τ_{h} identification efficiency. The trigger efficiency corrections are obtained from parametric fits to the trigger efficiency as a function of p_{T} derived for simulated events and data. The identification efficiency corrections are derived as a function of the p_{T} of the τ_{h} candidate. For $p_{\mathrm{T}}^{\tau_{\mathrm{h}}} > 40\,\mathrm{GeV}$, a correction is also derived for each τ_{h} decay mode individually, which is used only in the $\tau_h\tau_h$ final state. Corrections to the energy scale of the τ_h decays and of electrons misidentified as τ_h are derived for each data-taking year and each τ_h decay mode individually, from likelihood scans of discriminating observables, such as the reconstructed τ_h mass. For muons misidentified as τ_h, this effect has been checked to be negligible.

Corrections are applied to the magnitude and resolution of p_T^{miss} in τ-embedded events to account for a slight bias due to the imperfect removal of the energy deposits from the muons that are replaced by simulated τ decays during the embedding procedure. These corrections are derived by comparing p_T^{miss} in τ-embedded events with full event simulations.

The following corrections only apply to fully simulated events. During the 2016 and 2017 data taking, a gradual shift in the timing of the inputs of the ECAL L1 trigger in the region at $|\eta| > 2.0$ caused a specific trigger inefficiency [86]. For events containing an electron (a jet) with p_T larger than $\approx$50 ($\approx$100) GeV, in the region of $2.5 < |\eta| < 3.0$ the efficiency loss is 10–20%, depending on p_T, η, and time. Corresponding corrections have been derived from data and applied to the simulation, where this effect is not present.

The energies of jets are corrected to the expected response of the jet at the stable hadron level, using corrections measured in bins of the jet p_T and η. These corrections are usually not larger than 10–15%. Residual data-to-simulation corrections are applied to the simulated event samples. They usually range between subpercent level at high jet p_T in the central part of the detector to a few percent in the forward region. The energy resolution of simulated jets is also adjusted to match the resolution in data. A correction is applied to the direction and magnitude of $\vec{p}_T^{miss}$ based on differences between estimates of the hadronic recoil in $Z \to \mu\mu$ events in data and simulation. This correction is applied to the simulated Z boson, h, and ϕ signal events, where a hadronic recoil against a single particle is well defined. The efficiencies for genuine and misidentified b jets to pass the working points of the b jet identification discriminant, as given in Section 5, are determined from data, using $t\bar{t}$ events for genuine b jets and Z boson production in association with jets for jets originating from light quarks. Data-to-simulation corrections are obtained for these efficiencies and used to correct the number of b jets in the simulation.

Data-to-simulation corrections are further applied to simulated events in which an electron (muon) is reconstructed as a τ_h candidate, to account for residual differences in the $e(\mu) \to \tau_h$ misidentification rate between data and simulation. In a similar way, a correction is applied to account for residual differences in the $\mu \to e$ misidentification rate between data and simulation.

The dilepton mass and p_T spectra in simulated $Z/\gamma^* \to \ell\ell$ events are corrected to better match the data. To this purpose the dilepton mass and p_T are measured in data and simulation in $\mu\mu$ events, and the simulated events are corrected to match the spectra in data. In addition, all simulated $t\bar{t}$ events are weighted to better match the top quark p_T distribution observed in data [145]. The overall normalization of $t\bar{t}$ events is constrained by the $t\bar{t}$ control region described in Section 5.

7.2 Uncertainties related to the τ-embedding method or the simulation

The following uncertainties, related to the level of control of the reconstruction of electrons, muons, and τ_h candidates after selection, apply to simulated and τ-embedded events. Unless stated otherwise they are partially correlated across τ-embedded and simulated events. Uncertainties in the identification efficiency of electrons and muons amount to 2%, correlated across all years. Since no significant dependence on the p_T or η of each corresponding lepton is observed these uncertainties are introduced as normalization uncertainties. A similar reasoning applies to uncertainties in the electron and muon trigger efficiencies, which amount to 2% each. Due to differences in the trigger leg definitions they are treated as uncorrelated for single-lepton and pair triggers. This may result in shape-altering effects in the overall model, since both trigger types act on different regimes in lepton p_{T}.

For fully simulated events, an uncertainty in the electron energy scale is derived from the calibration of ECAL crystals, and applied on an event-by-event basis. For τ-embedded events, uncertainties of 0.5–1.25%, split by the ECAL barrel and endcap regions, are derived for the corrections described in Section 7.1. Due to the different ways the uncertainties are determined and differences in detector conditions they are treated as uncorrelated across simulated and τ-embedded events. They lead to shape-altering variations and are treated as correlated across years. The muon momentum (p^{μ}) is very precisely known. A variation within the given uncertainties, depending on the muon η and p_{T} has been checked to have no influence on the analysis.

Uncertainties in the τ_{h} identification efficiency are between 3–9% in bins of τ_{h} p_{T}. These uncertainties are statistically dominated and, therefore, are treated as uncorrelated across decay modes, p_{T} bins, and years. The same is true for the uncertainties in the τ_{h} energy scale, which amount to 0.2–1.1%, depending on the p_{T} and the decay mode of the τ_{h}. For the energy scale of electrons misidentified as τ_{h} candidates, the uncertainties are 1–6.5%. The uncertainty in the energy scale of muons misidentified as τ_{h} is 1%. Concerning correlations, the same statements apply as for the τ_{h} energy scale. Uncertainties in the τ_{h} trigger efficiency are typically $\mathcal{O}(10\%)$, depending on the p_{T} of the τ_{h}. They are obtained from parametric fits to data and simulation, and are treated as uncorrelated across triggers and years. All uncertainties discussed in this paragraph lead to shape-altering variations.

Three further sources of uncertainty are considered for τ-embedded events. A 4% normalization uncertainty accounts for the level of control in the efficiency of the $\mu\mu$ selection in data, which is unfolded during the τ-embedding procedure. The dominant part of this uncertainty originates from the trigger used for selection. Since these trigger setups differed across years, this uncertainty is treated as uncorrelated across years. Another shape- and normalization-altering uncertainty in the yield of $\mathrm{t\bar{t}} \to \mu\mu + \mathrm{X}$ decays, which are part of the τ-embedded event samples, ranges between subpercent level and 8%, depending on the event composition of the model. For this uncertainty, the number and shape of $\mathrm{t\bar{t}}$ events contained in the τ-embedded event samples are estimated from simulation, for which the corresponding decay has been selected at the parton level. This estimate is then varied by $\pm 10\%$. Finally, an uncertainty in the $p_{\mathrm{T}}^{\mathrm{miss}}$ correction for the τ-embedded events described in Section 7.1 is applied. As this correction is derived from a comparison to full event simulation, this uncertainty is related to the imperfect $p_{\mathrm{T}}^{\mathrm{miss}}$ reconstruction in simulation.

For fully simulated events, the following additional uncertainties apply. Uncertainties in the $\mathrm{e}(\mu) \to \tau_{\mathrm{h}}$ misidentification rate are 18–41% for electrons and 7–67% for muons, depending on the η of the τ_{h} candidate. These uncertainties only apply to simulated $\mathrm{Z} \to \mathrm{ee}$ ($\mathrm{Z} \to \mu\mu$) events, which are of marginal importance for the analysis. The same is true for the uncertainty in the reweighting in the $\mathrm{Z}/\gamma^{*} \to \ell\ell$ dilepton mass and p_{T}, discussed in Section 7.1, which is typically smaller than 1%. A normalization uncertainty due to the timing shift of the inputs of the ECAL L1 trigger described in Section 7.1 amounts to 2–3%.

Uncertainties in the energy calibration and resolution of jets are applied with different correlations depending on their sources, comprising statistical limitations of the measurements used for calibration, the time-dependence of the energy measurements in data due to detector ageing, and bias corrections introduced to cover residual differences between simulation and data. They range between subpercent level and $\mathcal{O}(10\%)$, depending on the kinematic properties of the jets in the event. Similar uncertainties are applied for the identification rates for b jets and for the misidentification rates for light quark- or gluon-induced jets, which are each of a similar range.

Depending on the process under consideration, two independent uncertainties in $p_{\mathrm{T}}^{\mathrm{miss}}$ are applied. For processes that are subject to recoil corrections, i.e., Z boson, h, or ϕ production, uncertainties in the calibration and resolution of the hadronic recoil are applied, they typically result in changes to the event yields ranging from 0–5%. For all other processes, an uncertainty in $p_{\mathrm{T}}^{\mathrm{miss}}$ is derived from the amount of unclustered energy in the event.

The integrated luminosities of the 2016, 2017, and 2018 data-taking periods are individually known with uncertainties in the 1.2–2.5% range [146–148], while the total integrated luminosity for the years 2016–2018 has an uncertainty of 1.6%, the improvement in precision reflecting the (uncorrelated) time evolution of some systematic effects. Uncertainties in the predictions of the cross sections for simulated backgrounds amount to 5% for diboson and single t production [121–123] and 2% for Z boson production [119]. These uncertainties are correlated across years. A shape-altering uncertainty is derived in the reweighting of the top quark p_{T} described in Section 7.1 by applying the correction twice or not applying it at all. This uncertainty has only a very small effect on the final discriminant.

Theoretical uncertainties in the acceptance of bbϕ signal events are obtained from variations of the renormalization (μ_{R}) and factorization (μ_{F}) scales, the h_{damp} factor, and the PDFs. The scale uncertainty is obtained from the envelope of the six variations of μ_{R} and μ_{F} by factors of 0.5 and 2, as recommended in Ref. [149]. The scale h_{damp} is varied by factors of $1/\sqrt{2}$ and $\sqrt{2}$. The uncertainty from the variation of μ_{R} and μ_{F}, and the uncertainty from the variation of h_{damp} are added linearly, following the recommendation in Ref. [149], resulting in an overall uncertainty that ranges from 1–8% (1–5%) for the (no) b-tag categories depending on the tested mass. The PDF uncertainty ranges from 1–2%.

Uncertainties in the acceptance of the ggϕ process are also obtained from variations of μ_{R}, μ_{F}, and h_{damp}. The μ_{R} and μ_{F} scales are varied as described above for the bbϕ process, whereas the h_{damp} scale is varied by factors of 0.5 and 2 as suggested in Ref. [131]. The influence of the former (latter) variation on the signal acceptance amounts to 20% (35%) in the most extreme cases (i.e. for the smallest m_{ϕ} values). For larger m_{ϕ} values, the variation is at the subpercent level. In both cases the uncertainties also result in shape-altering effects in the overall model.

For the parameter scan in the MSSM interpretations, theoretical uncertainties in the ggϕ and bbϕ cross sections are included, as described in Ref. [84]. This includes uncertainties in the μ_{R} and μ_{F} scales, the PDF, and α_{S}. The uncertainties are evaluated separately for each m_{A}-$\tan\beta$ point under consideration. They are typically 5–20% (10–25%) for ggϕ (bbϕ) production.

Theoretical uncertainties in the U_1 signal process include uncertainties in the μ_{R} and μ_{F} scales, the PDF, α_{S}, the scale Q_{match}, the parton shower modelling, the $\beta_{\mathrm{L}}^{s\tau}$ parameter, and the flavour scheme choice. The uncertainty due to the μ_{R} and μ_{F} scale variations is about 15%. The uncertainties due to the PDFs and α_{S} variations are about 15% and 4%, respectively. The Q_{match} and parton shower uncertainties predominantly affect the signal acceptances in the (no) b-tag categories, with magnitudes of about 11% and 1% (5% and 6%), respectively. The uncertainty in the $\beta_{\mathrm{L}}^{s\tau}$ parameter is estimated by varying the coupling strength by the uncertainties obtained in the fit to the low-energy observables presented in Ref. [70] and summarized in Table 1. The resulting uncertainty varies the signal yields by 4–12%. The uncertainty in the signal acceptance due to the choice of flavour scheme is estimated by comparing the predictions in the 4FS and 5FS calculations, which mainly affect the $N_{\text{b-jets}}$ distribution. The resulting uncertainty has a magnitude of 25% (18%) for the (no) b-tag categories.

For all results shown in the following, the SM Higgs boson production is taken into account in the statistical model. Uncertainties due to different choices of μ_R and μ_F for the calculation of the production cross section of the SM Higgs boson amount to 3.9% for gluon fusion, 0.4% for VBF, 2.8% for Zh, and 0.5% for Wh production [124–126, 150, 151]. Uncertainties due to different choices for the PDFs and α_S amount to 3.2% for gluon fusion, 2.1% for VBF, 1.6% for Zh, and 1.9% for Wh production.

7.3 Uncertainties related to jets misidentified as an electron, muon, or τ_h

For the F_F-method, the following uncertainties apply. The F_F^i and their corrections are subject to statistical fluctuations in each corresponding DR^i. The corresponding uncertainties are split into a normalization and a shape-altering part and propagated into the final discriminant. They are typically 1–10% and are treated as uncorrelated across the kinematic and topological bins in which they are derived. An additional uncertainty is defined by varying the choice of the functional form for the parametric fits.

Uncertainties are also applied to cover bias corrections and extrapolation factors, varying from a few percent to $\mathcal{O}(10\%)$, depending on the kinematic properties of the τ_h candidate and the topology of the event. These are both normalization and shape-altering uncertainties.

An additional source of uncertainty concerns the subtraction of processes other than the enriched process in each corresponding DR^i. These are subtracted from the data using simulated or τ-embedded events. The combined shape of the events to be removed is varied by 10%, and the measurements are repeated. The impacts of these variations are then propagated to the final discriminant as shape-altering uncertainties.

An uncertainty in the estimation of the three main background fractions in the AR is estimated from a variation of each individual contribution also by 10%, increasing or decreasing the remaining fractions such that the sum of all contributions remains unchanged. The amount of variation is motivated by the uncertainty in the production cross sections and acceptances of the involved processes and the constraint on the process composition that can be clearly obtained from the AR. The effect of this variation is observed to be very small, since usually one of the contributions dominates the event composition in the AR.

Since the background from QCD multijet events in the eμ final state is also determined from a DR, uncertainties that account for the statistical uncertainty in the data and the subtracted backgrounds in this DR are applied in a similar way. These uncertainties amount to 2–4%. In addition, this background is subject to uncertainties related to the extrapolations from the DR to the corresponding SRs. These uncertainties are $\mathcal{O}(10\%)$ depending on p_T^e, p_T^μ, and $N_{\text{b-jets}}$. Due to their mostly statistical nature, all uncertainties related to the F_F-method and SS-methods are treated as uncorrelated across years.

In the eμ channel the subdominant contribution to the jet $\to \ell$ and $\mu \to$ e backgrounds is estimated from simulation. Uncertainties in the simulated jet $\to$ e and jet $\to \mu$ misidentification rates are 10 and 12%, respectively. They are treated as correlated across years. The uncertainty in the $\mu \to$ e misidentification rate is 15–45%, and is treated as uncorrelated across years as it is mostly statistical in nature. A summary of all systematic uncertainties that have been discussed in this section is given in Table 6.

Table 6: Summary of systematic uncertainties discussed in the text. The first column indicates the source of uncertainty; the second the processes that it applies to; the third the variation; and the last how it is correlated with other uncertainties. A checkmark is given also for partial correlations. More details are given in the text.

Uncertainty		Process				Variation	Correlated across	
		Sim.	τ-emb.	F_F	SS		Years	Processes
τ-emb.	Acceptance	—	✓	—	—	4%	—	—
	$t\bar{t}$ fraction	—	✓	—	—	0.1–8%	—	—
μ	ID	✓	✓	—	—	2%	✓	✓
	Trigger	✓	✓	—	—	2%	—	✓
e	ID	✓	✓	—	—	2%	✓	✓
	Trigger	✓	✓	—	—	2%	—	✓
	Energy scale	✓	✓	—	—	See text	✓	✓
τ_h	ID	✓	✓	—	—	3–8%	—	✓
	Trigger	✓	✓	—	—	5–10%	—	✓
	Energy scale	✓	✓	—	—	0.2–1.1%	—	✓
$\mu \to \tau_h$	Miss-ID	✓	—	—	—	7–67%	—	—
	Energy scale	✓	—	—	—	1%	—	—
$e \to \tau_h$	Miss-ID	✓	—	—	—	18–41%	—	—
	Energy scale	✓	—	—	—	1–6.5%	—	—
Jet $\to$ e miss-ID		✓	—	—	—	10%	✓	✓
Jet $\to \mu$ miss-ID		✓	—	—	—	10%	✓	✓
$\mu \to$ e Miss-ID		✓	—	—	—	15–45%	—	✓
Z boson p_T reweighting		✓	—	—	—	<1%	✓	—
Jet energy scale & resolution		✓	—	—	—	0.1–10%	✓	✓
b-jet (miss-)ID		✓	—	—	—	1–10%	—	✓
p_T^{miss} calibration		✓	—	—	—	See text	✓	✓
ECAL timing shift		✓	—	—	—	2–3%	✓	✓
t quark p_T reweighting		✓	—	—	—	See text	✓	—
Luminosity		✓	—	—	—	1.2–2.5%	✓	✓
Background cross sections		✓	—	—	—	2–5%	✓	—
Signal theory uncertainties		✓	—	—	—	See text	✓	—
F_F	Statistics	—	—	✓	—	$\mathcal{O}$(1–10%)	—	—
	Corrections	—	—	✓	—	$\mathcal{O}$(10%)	—	—
	Non-F_F processes	—	—	✓	—	10%	—	—
	F_F proc. composition	—	—	✓	—	10%	—	—
QCD (eμ)	Statistics	—	—	—	✓	2–4%	—	—
	AR to SR Extrapolations	—	—	—	✓	$\mathcal{O}$(10%)	—	—

8 Results

The statistical model used to infer the signal from the data is defined by an extended binned likelihood of the form

$$\mathcal{L}\left(\{k_i\},\{\mu_s\},\{\theta_j\}\right) = \prod_i \mathcal{P}\left(k_i | \sum_s \mu_s\, S_{si}(\{\theta_j\}) + \sum_b B_{bi}(\{\theta_j\})\right) \prod_j \mathcal{C}(\tilde{\theta}_j|\theta_j), \quad (12)$$

where i labels the bins of the discriminating distributions of all categories, split by $\tau\tau$ final state and data-taking year. The function $\mathcal{P}(k_i|\sum \mu_s\, S_{si}(\{\theta_j\}) + \sum B_{bi}(\{\theta_j\}))$ corresponds to the Poisson probability to observe k_i events in bin i for a prediction of $\sum \mu_s\, S_{si}$ signal and $\sum B_{bi}$ background events. The predictions for S_{si} and B_{bi} are obtained from the signal and background models discussed in Section 6. The parameters μ_s act as linear scaling parameters of the corresponding signal s. Systematic uncertainties are incorporated in the form of penalty terms for additional nuisance parameters $\{\theta_j\}$ in the likelihood, appearing as a product with predefined probability density functions $\mathcal{C}(\tilde{\theta}_j|\theta_j)$, where $\tilde{\theta}_j$ corresponds to the nominal value for θ_j. The predefined uncertainties in the $\tilde{\theta}_j$, as discussed in Section 7, may be constrained by the fit to the data.

The test statistic used for the inference of the signal is the profile likelihood ratio as discussed in Refs. [152, 153]:

$$q_{\mu_s} = -2\ln\left(\frac{\mathcal{L}(\{k_i\}|\sum\limits_s \mu_s\, S_{si}(\{\hat{\theta}_{j,\mu_s}\}) + \sum\limits_b B_{bi}(\{\hat{\theta}_{j,\mu_s}\}))}{\mathcal{L}(\{k_i\}|\sum\limits_s \hat{\mu}_s\, S_{si}(\{\hat{\theta}_{j,\hat{\mu}_s}\}) + \sum\limits_b B_{bi}(\{\hat{\theta}_{j,\hat{\mu}_s}\}))}\right), \quad 0 \leq \hat{\mu}_s \leq \mu_s\,, \quad (13)$$

where one or more parameters μ_s are the parameters of interest (POIs) and $\hat{\mu}_s$, $\hat{\theta}_{j,\mu_s}$, and $\hat{\theta}_{j,\hat{\mu}_s}$ are the values of the given parameters that maximize the corresponding likelihood. The index of q_{μ_s} indicates that the test statistic is evaluated for a fixed value of μ_s. In the large number limit, the sampling distribution of q_{μ_s} can be approximated by analytic functions, from which the expected median and central intervals can be obtained as described in Ref. [154]. The signal is inferred from the data in three different ways:

i) the model-independent ϕ search features a signal model for a single narrow resonance ϕ with a width negligible compared to the experimental resolution, in addition to h_{obs};

ii) for the search for vector leptoquarks, the data are interpreted in terms of the non-resonant U_1 t-channel exchange;

iii) the interpretation of the data in terms of MSSM benchmark scenarios relies on three resonances in the $\tau\tau$ mass spectrum with mass values and rates determined by the parameters of the corresponding scenario.

Detailed descriptions of the specific statistical procedures and the results obtained in each case are given in the following sections.

8.1 Model-independent ϕ search

For the model-independent ϕ search, we investigate $gg\phi$ and $bb\phi$ production corresponding to two independent POIs $\mu_{gg\phi}$ and $\mu_{bb\phi}$ in the likelihood of Eq. (12). In the model, h_{obs} is treated as background assuming production cross sections and branching fraction to τ leptons as expected from the SM. For $m_\phi \geq 250\,\text{GeV}$, the signal extraction is based on binned template distributions of m_T^tot in the 17 high-mass categories per data-taking year shown in Fig. 4, resulting in a total of 51 input distributions for signal extraction. For $60 \leq m_\phi < 250\,\text{GeV}$, binned template distributions of $m_{\tau\tau}$ are used in the 26 low-mass categories shown in Fig. 5, resulting in 78 input distributions for signal extraction. A few examples of these input distributions in a subset of the most sensitive categories per final state are shown in Figs. 7 and 8. In each figure the expected background distributions are represented by the stack of filled histograms in the upper panel of each subfigure, where each filled histogram corresponds to a process as discussed in Section 6. The grey shaded band associated with the sum of filled histograms corresponds to the combination of all uncertainties discussed in Section 7, including all correlations as obtained from the fit of the background model to the data. In the lower panel of each subfigure the ratio of the data points over the expectation from the background model is shown. The statistical uncertainty in the data is represented by the error bars and the uncertainty in the sum of all background processes, after the fit to the data, by the shaded band. The expected m_T^tot ($m_{\tau\tau}$) distributions for a ggϕ or bbϕ signal with $m_\phi = 1200\,(100)\,\text{GeV}$ are also shown.

In Fig. 9 the expected and observed 95% confidence level (CL) upper limits on the product of the cross sections and branching fraction into τ leptons for ggϕ and bbϕ production in a mass range of $60 \leq m_\phi \leq 3500\,\text{GeV}$ are shown. These limits have been obtained following the modified frequentist approach described in Refs. [155, 156]. When setting the limit in one production mode the POI of the other production mode is profiled. The limits are shown split by the low- ($m_\phi < 250\,\text{GeV}$) and high-mass ($m_\phi \geq 250\,\text{GeV}$) region of the search.

The expected limits in the absence of a signal span four orders of magnitude between $\approx$10 pb (at $m_\phi = 60\,\text{GeV}$) and $\approx$0.3 fb (at $m_\phi = 3.5\,\text{TeV}$) for both production modes, with a falling slope for increasing values of m_ϕ. In general, the observation falls within the central 95% central interval of the expectation. For the low-mass search, the largest deviation from the expectation is observed for ggϕ production at $m_\phi = 100\,\text{GeV}$ with a local (global) p-value of 3.1 (2.7) standard deviations (s.d.). The best fit value of the cross section is $\sigma_{\text{gg}\phi}\,\mathcal{B}(\phi \to \tau\tau) = (5.8\pm^{2.4}_{2.0})\,\text{pb}$. The excess at $m_\phi = 100\,\text{GeV}$ exhibits a p-value of 50% (58%) for the compatibility across $\tau\tau$ final states (data-taking years). Within the resolution of $m_{\tau\tau}$ it coincides with a similar excess seen in a previous search for low-mass resonances by the CMS Collaboration in the $\gamma\gamma$ final state using data collected during the 2016 (2012) LHC running period at $\sqrt{s} = 13$ (8) TeV, corresponding to an integrated luminosity of 35.9 (19.7) fb^{-1} [157]. In this case, the smallest local p-value corresponds to a significance of 2.8 s.d. for a mass of 95.3 GeV. An updated search in the $\gamma\gamma$ final state by the CMS Collaboration is in progress including additional data collected during the 2017–2018 LHC running period. We note that the local (global) significance for the $\tau\tau$ search evaluated at a similar mass value of $m_\phi = 95\,\text{GeV}$ is 2.6 (2.3) s.d. and the best fit value of the cross section is $\sigma_{\text{gg}\phi}\,\mathcal{B}(\phi \to \tau\tau) = (7.7\pm^{3.9}_{3.1})\,\text{pb}$. For the high-mass search, the largest deviation from the expectation is observed for ggϕ production at $m_\phi = 1.2\,\text{TeV}$ with a local (global) p-value of 2.8 (2.4) s.d. , where the best fit value of the cross section is $\sigma_{\text{gg}\phi}\,\mathcal{B}(\phi \to \tau\tau) = (3.1 \pm 0.1)\,\text{fb}$. The excess at $m_\phi = 1.2\,\text{TeV}$ exhibits a p-value of 11% (64%) for the compatibility across $\tau\tau$ final states (data-taking years). For bbϕ production, no deviation from the expectation beyond the level of 2 s. d. is observed. In Fig. 10 the same results are presented in the form of maximum likelihood estimates with 68 and 95% CL contours obtained from scans of the signal likelihood which show the best fit values of the ggϕ and bbϕ cross sections for selected values of m_ϕ between 60 GeV and 3.5 TeV.

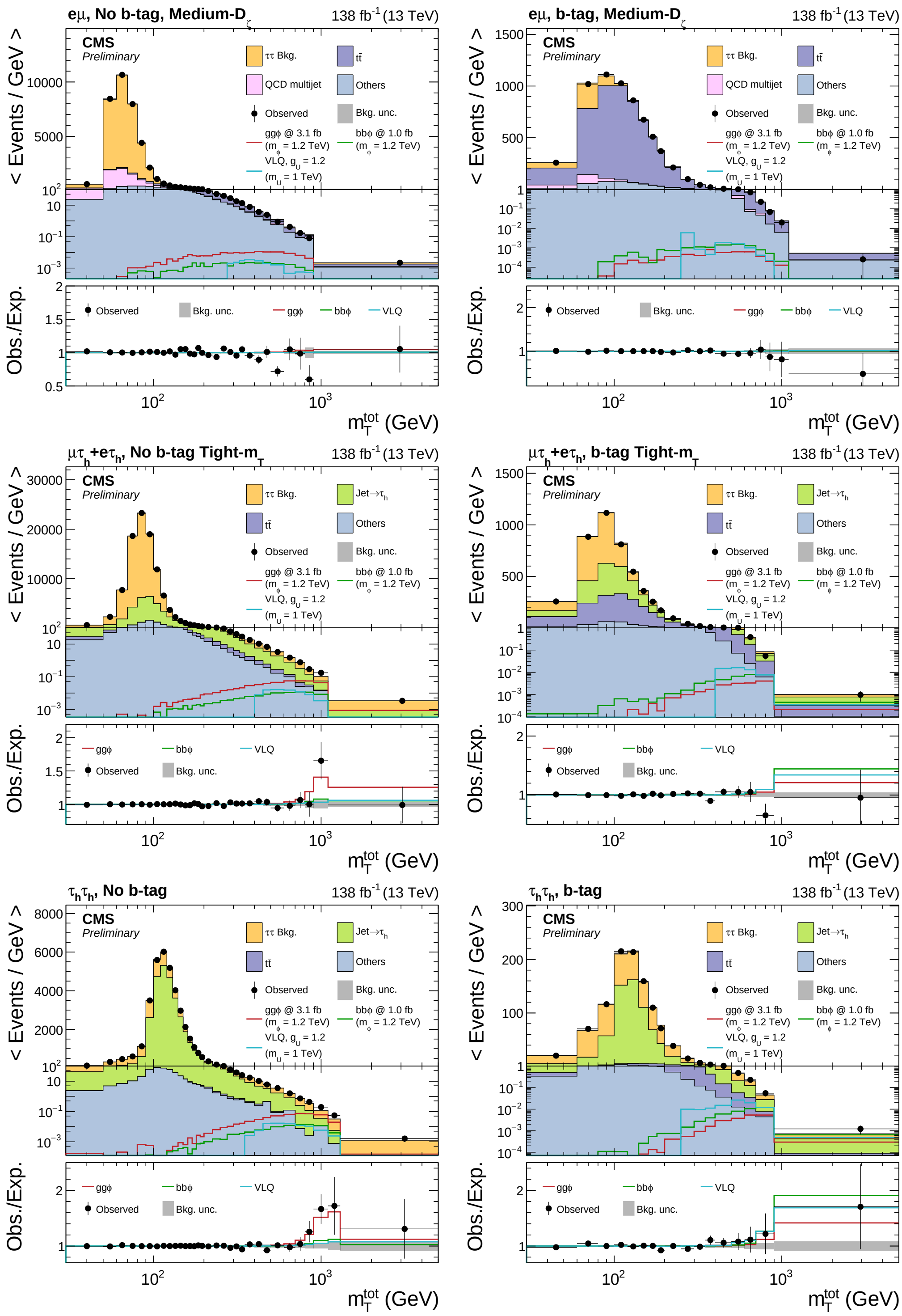

Figure 7: Distributions of $m_{\mathrm{T}}^{\mathrm{tot}}$ in the global (left) no b-tag and (right) b-tag categories in the (upper row) eμ, (middle row) eτ_{h} and $\mu\tau_{\mathrm{h}}$, and (lower row) $\tau_{\mathrm{h}}\tau_{\mathrm{h}}$ final states, for the most signal sensitive categories. For the eμ final state, the Medium-D_{ζ} category is displayed, for the eτ_{h} and $\mu\tau_{\mathrm{h}}$ final states the Tight-m_{T} categories are shown. The black horizontal line in the upper panel of each subfigure indicates the change from logarithmic to linear scale on the vertical axis. The distributions are shown for all data-taking years combined.

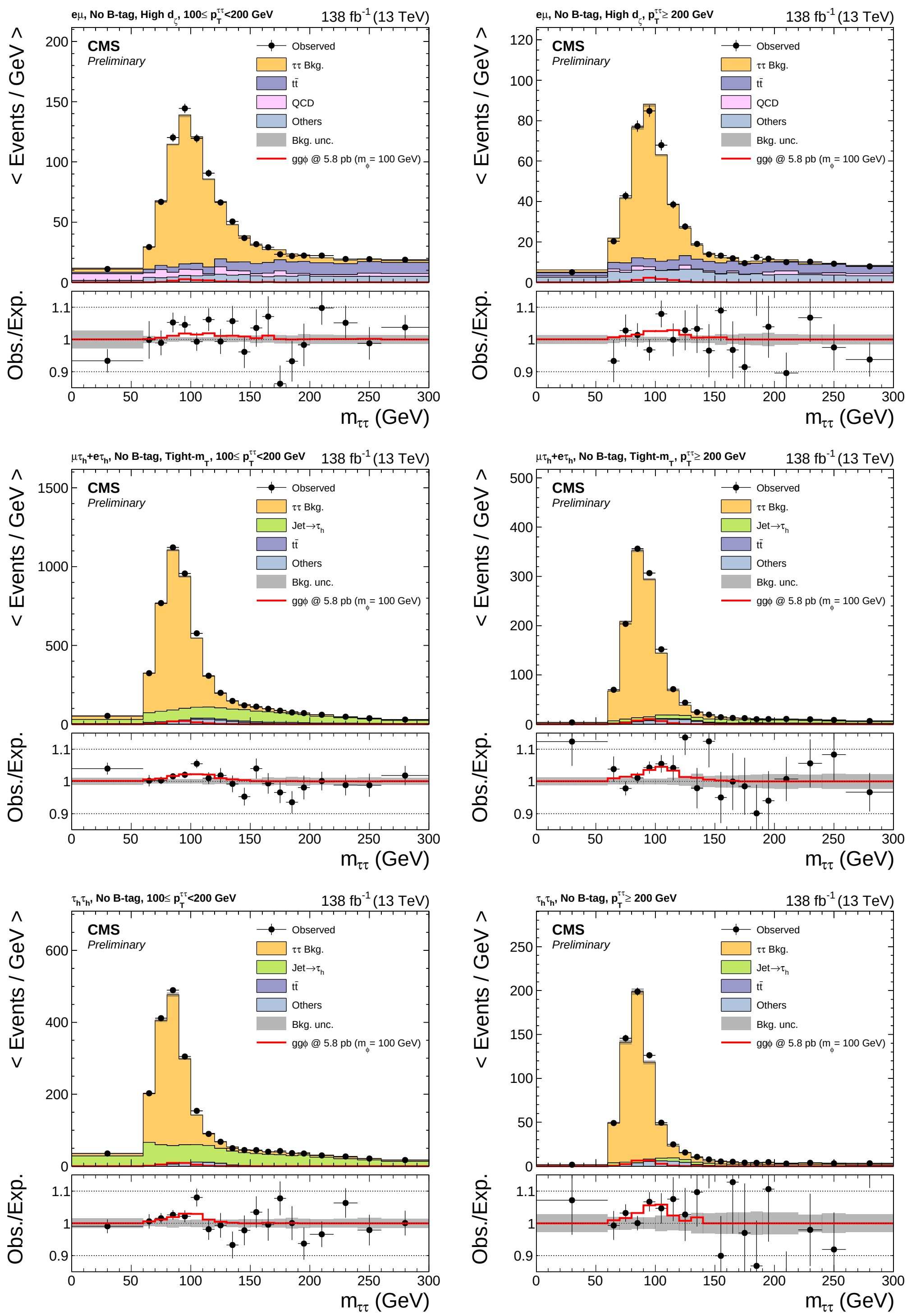

Figure 8: Distributions of $m_{\tau\tau}$ in the most signal sensitive categories: the $100 \leq p_{\mathrm{T}}^{\tau\tau} < 200\,\mathrm{GeV}$ (left) and $p_{\mathrm{T}}^{\tau\tau} \geq 200\,\mathrm{GeV}$ (right) categories of the global no b-tag category used for the model-independent ϕ search for $60 \leq m_{\phi} < 250\,\mathrm{GeV}$ for the (upper row) $\mathrm{e}\mu$, (middle row) $\mathrm{e}\tau_{\mathrm{h}}$ and $\mu\tau_{\mathrm{h}}$, and (lower row) $\tau_{\mathrm{h}}\tau_{\mathrm{h}}$ final states. The distributions are shown for all data-taking years combined.

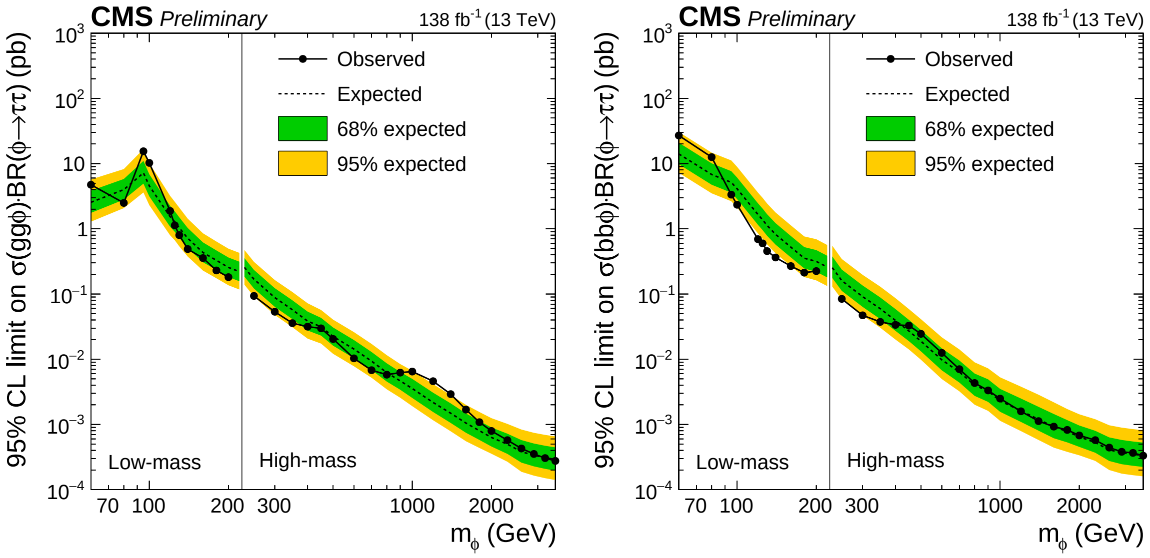

Figure 9: Expected and observed 95% CL upper limits on the product of the cross sections and branching fraction into τ leptons for ggϕ and bbϕ production in a mass range of $60 \leq m_\phi \leq 3500\,\text{GeV}$, in addition to h_obs. The expected median of the exclusion limit in the absence of signal is shown by the dashed line. The dark green and bright yellow bands indicate the 68 and 95% central intervals for the expected exclusion limit. The black dots correspond to the observed limits.

8.2 Search for vector leptoquarks

The inputs for the search for vector leptoquarks are the binned template distributions of m_T^tot in the high-mass categories, shown in Fig. 4, resulting in 51 input distributions for signal extraction, for the years 2016–2018. Based on these inputs a signal is searched for in the range $1 \leq m_\text{U} \leq 5\,\text{TeV}$.

As discussed in Section 6.4, the U_1 t-channel exchange may reduce or enhance the yields in the m_T^tot template distributions used for signal extraction with respect to the expectation from the background model, due to the destructive interference with the $\text{Z}/\gamma^* \to \tau\tau$ process. An example of this effect for a signal with $m_\text{U} = 1\,\text{TeV}$, $g_\text{U} = 1.5$, for the VLQ BM 1 scenario is shown in Fig. 6, right. From this figure a sizeable reduction in the yield of $\tau\tau$ events is observed for $m_\text{T}^\text{tot} \lesssim 300\,\text{GeV}$ and a smaller excess for $300 \lesssim m_\text{T}^\text{tot} \lesssim 1000\,\text{GeV}$. In principle, the bins predicting event deficits with respect to the SM background contribute to the sensitivity of the analysis as well as the bins predicting excesses. However, the bins with deficits occur at smaller values of m_T^tot where the background is much larger and thus they don't contribute significantly to the overall sensitivity. Most of the sensitivity to the U_1 signal instead comes from the highest m_T^tot bins due to the smaller background yields. While reduced due to the destructive interference the signal yields tend to remain positive in these bins. The overall effect of the interference term is thus to reduce the analysis sensitivity compared to the expectation without interference effects included.

No statistically significant signal is observed and 95% CL upper limits on g_U are derived for the VLQ BM 1 and 2 scenarios, as shown in Fig. 11. The expected sensitivity of the analysis drops for increasing values of m_U following a linear progression with values from $g_\text{U} = 1.3$ (0.8) to 5.6 (3.2) for the VLQ BM 1 (2) scenario. The observed limits fall within the central 95% interval for the expected limit in the absence of signal. The expected limits are also within the 95% confidence interval of the best-fit results reported by Ref. [70], indicating that the search is

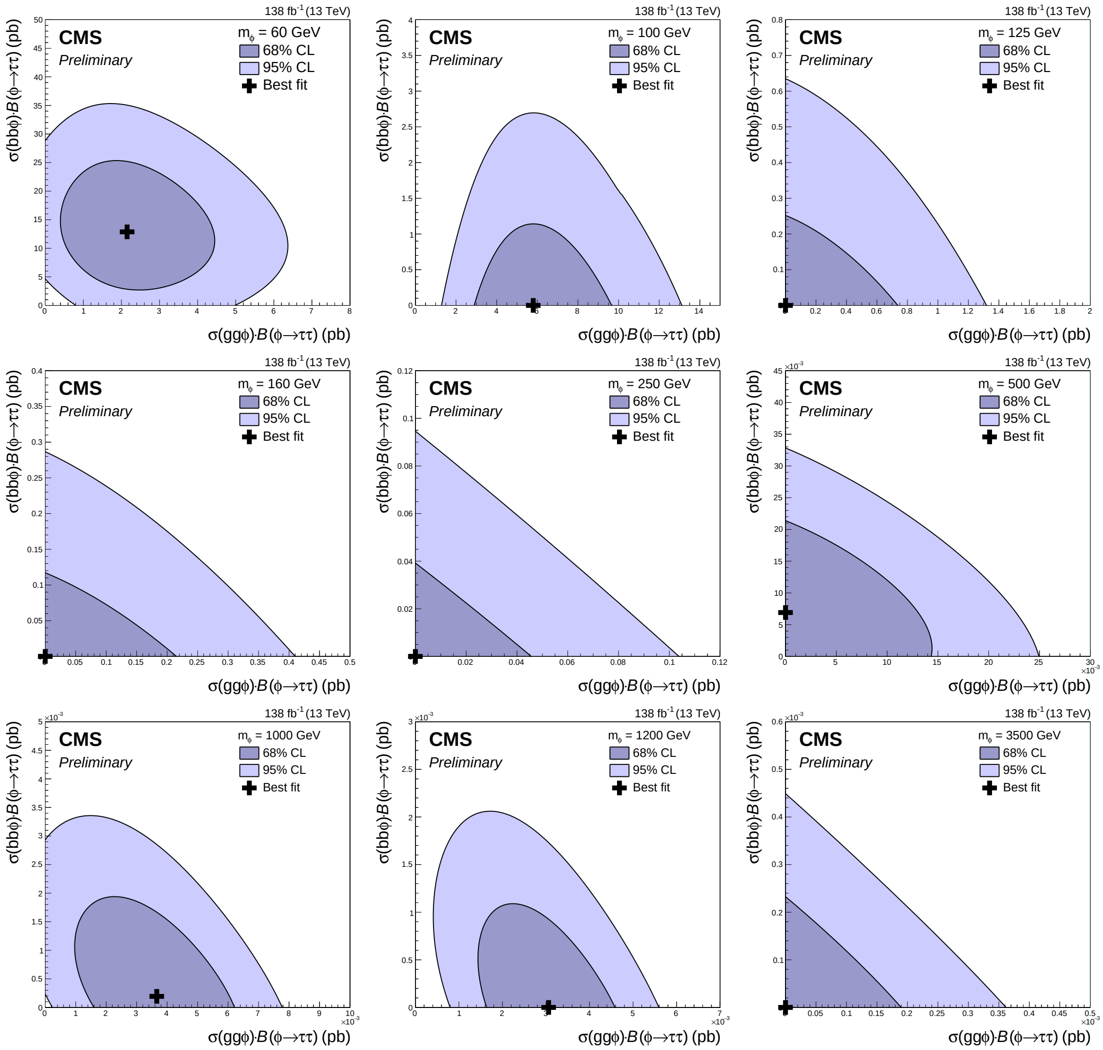

Figure 10: Maximum likelihood estimates, and 68 and 95% confidence level contours obtained from scans of the signal likelihood for the model-independent ϕ search. The scans are shown for selected values of m_{ϕ} between 60 GeV and 3.5 TeV.

sensitive to a portion of the parameter space that can explain the B-physics anomalies.

8.3 MSSM interpretation of the data

For the interpretation of the data in MSSM benchmark scenarios, the signal is based on the binned distributions of $m_{\mathrm{T}}^{\mathrm{tot}}$ in the high-mass categories shown in Fig. 4, complemented by distributions of the NN output function following the strategy used for the cross section measurements in Ref. [105], as discussed in Section 5.2, resulting in 129 input distributions for signal extraction.

In the MSSM, the signal constitutes a multiresonance structure with contributions from h, H, and A. For the scenarios chosen for this note h is associated with h_{obs}. Any MSSM prediction has to match the observed properties of h_{obs}, in particular its mass, cross sections for various production modes, and branching fraction to τ leptons. For the benchmark scenarios summarized in Ref. [84], all model parameters have been chosen such that m_{h} is compatible with the observed h_{obs} mass of 125.38 GeV [4], within an uncertainty of ± 3 GeV in most of the provided parameter space. The uncertainty of ± 3 GeV in the prediction of m_{h} is supposed to reflect the

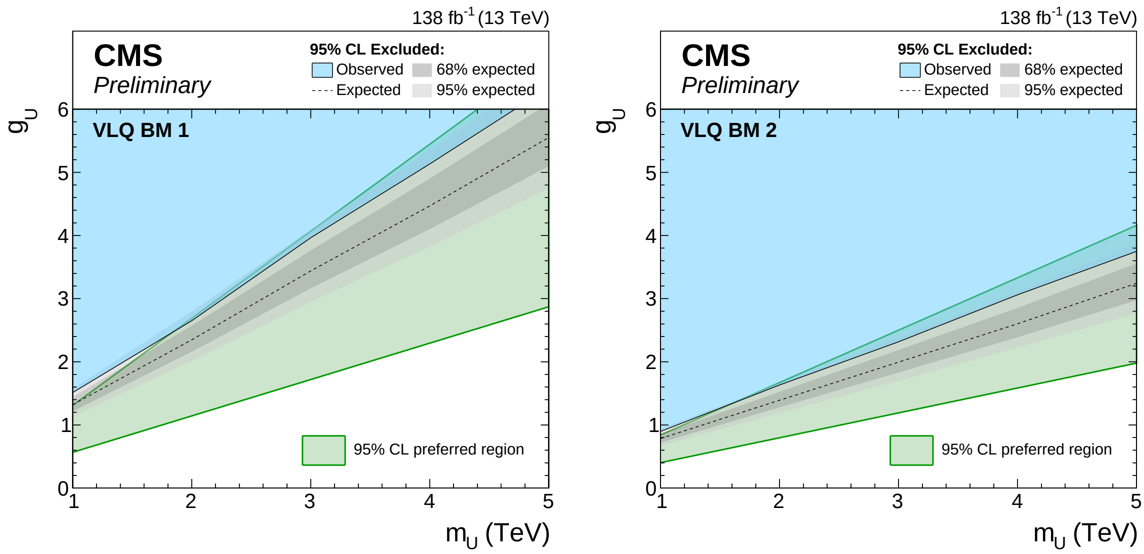

Figure 11: Expected and observed 95% CL upper limits on g_U in the VLQ BM 1 (left) and 2 (right) scenarios, in a mass range of $1 \leq m_U \leq 5\,\text{TeV}$. The expected median of the exclusion limit in the absence of signal is shown by the dashed line. The dark and bright grey bands indicate the central 68 and 95% intervals of the expected exclusion limit. The observed excluded parameter space is indicated by the coloured blue area. For both scenarios, the 95% confidence interval for the preferred region from the global fit of the low-energy observables presented in Ref. [70] is also shown by the green shaded area.

unknown effect of higher-order corrections as discussed in Ref. [158]. Assuming a flat Bayesian prior, m_h is allowed to take any value within these boundaries. For the interpretation this is taken into account by simulating the h signal at the observed h_{obs} mass. For h production, gluon fusion (ggh), b associated production (bbh), VBF, and Vh production are taken into account, and all cross sections and the branching fraction into τ leptons are scaled according to the MSSM predictions. To remove any dependencies of these predictions on the exact value of m_h, they are scaled to the expectation for $m_h = 125.38\,\text{GeV}$, following the prescription of Ref. [84]. For A and H production, gluon fusion (ggA, ggH) and b associated production (bbA, bbH) are taken into account.

All kinematic distributions are modelled within the accuracies discussed in Section 6.4. In particular, the p_T spectra of ggH and ggA production are modelled as a function of $\tan\beta$ for each tested value of m_A, resulting in softer progression for increasing values of $\tan\beta$. In the high-mass no b-tag categories the h signal is expected to be negligible. It is therefore dropped from the signal templates. A summary of the association of signals to the templates used for signal extraction is given in Table 7. To interpolate the simulated mass points to the exact predicted values of m_H and m_A a linear template morphing algorithm, as described in Ref. [159], is used.

Table 7: Contribution of MSSM signals to the m_T^{tot} and NN output function template distributions used for signal extraction for the interpretation of the data in MSSM benchmark scenarios.

Categories		Signal processes: ggh, bbh, VBF, Vh	Signal processes: ggH/ggA, bbH/bbA
No b-tag	$m_{\tau\tau} < 250\,\text{GeV}$	✓	✓
No b-tag	$m_{\tau\tau} \geq 250\,\text{GeV}$	—	✓
B-tag		✓	✓
Control regions		✓	—

Finally, the $m_{\rm A}$-$\tan\beta$ plane is scanned and for each tested point in ($m_{\rm A}$, $\tan\beta$) the $\rm CL_s$ value is calculated. Those points where $\rm CL_s$ falls below 5% define the 95% CL exclusion contour for the benchmark scenario under consideration. The underlying test compares the MSSM hypothesis, with signal contributions for h ($S_{\rm h}$), H ($S_{\rm H}$), and A ($S_{\rm A}$), with the SM hypothesis ($S_{\rm SM}$), with only one signal contribution related to $\rm h_{obs}$. The test versus the SM hypothesis is justified by the properties of $\rm h_{obs}$ being in agreement with the SM expectation within the experimental accuracy of current measurements. For the hypothesis test the likelihood of Eq. (12) is expressed in the form

$$\mathcal{L}\left(\{k_i\},\mu\right) = \prod_i \mathcal{P}\Big(k_i|\mu\Big((S_{\rm h}-S_{\rm SM})+S_{\rm H}+S_{\rm A}\Big)+S_{\rm SM}+\sum_b B_b\Big), \tag{14}$$

where for brevity the dependence on the nuisance parameters $\{\theta_j\}$ has been omitted. Equation (14) represents a nested likelihood model from which the MSSM hypothesis (with $\mu = 1$) evolves through continuous transformation from the SM hypothesis (with $\mu = 0$). We note that the only physically meaningful hypotheses in Eq. (14) correspond to $\mu = 0$ and 1. On the other hand, in the large number limit this construction allows the application of the asymptotic formulas given in Ref. [154], as analytic estimates of the sampling distributions for the MSSM and SM hypotheses, when using the profile likelihood ratio given in Eq. (13) as the test statistic. We have verified the validity of the large number limit for masses of $m_{\rm A} \geq 1$ TeV with the help of ensemble tests. Since we are using the same template distributions for $S_{\rm SM}$ and $S_{\rm h}$ the transition from $\mu = 0$ to 1 corresponds to a normalization change of the signal contribution related to $\rm h_{obs}$, only.

In Fig. 12 the exclusion contours in the $m_{\rm A}$-$\tan\beta$ plane for two representative benchmark scenarios of the MSSM, $M_{\rm h}^{125}$ [81] and $M_{\rm h,EFT}^{125}$ [83], are shown. The red hatched areas indicate the regions where the compatibility of $m_{\rm h}$ with the observed $\rm h_{obs}$ mass could not be achieved within the previously discussed ± 3 GeV boundary. For low values of $\tan\beta$, higher scales of $m_{\rm SUSY}$ are required to accomplish a mass of $m_{\rm h} \approx 125$ GeV leading to large logarithmic terms in the higher-order corrections for $m_{\rm h}$. For the $M_{\rm h,EFT}^{125}$ scenario, these large logarithmic terms have been resummed using an effective field theory approach. The $M_{\rm h,EFT}^{125}$ can thus be viewed as a continuation of the $M_{\rm h}^{125}$ scenario for $\tan\beta \lesssim 10$.

For both scenarios the Higgs boson masses, mixing angle α, and effective Yukawa couplings have been calculated with the code FEYNHIGGS [160–167]. Branching fractions to τ leptons and other final states have been obtained from a combination of the codes FEYNHIGGS (and HDECAY [168, 169]) for the $M_{\rm h,EFT}^{125}$ ($M_{\rm h}^{125}$) scenario, as described in Ref. [84] following the prescriptions given in Refs. [149, 170, 171].

Inclusive cross sections for the production via gluon fusion have been calculated using the program SUSHI 1.7.0 [172, 173], including NLO corrections in $\alpha_{\rm S}$ for the t- and b-quark contributions to the cross section [174, 175], NNLO corrections in $\alpha_{\rm S}$ in the heavy t-quark limit, for the t-quark contribution [176–180], and next-to-NNLO contributions in $\alpha_{\rm S}$ for h production [181–183]. Electroweak corrections mediated by light quarks have been taken into account at two-loop accuracy reweighting the SM results of Refs. [184, 185]. Contributions from squarks and gluinos have been taken into account at NLO precision in $\alpha_{\rm S}$ following Refs. [186–188]. The $\tan\beta$-enhanced SUSY contributions to the Higgs-b couplings have been resummed using the one-loop $\Delta_{\rm b}$ terms from Ref. [189] as provided by FEYNHIGGS.

For b quark associated production, cross sections have been calculated for the SM Higgs boson as a function of its mass, based on soft-collinear effective theory [190, 191]. These cross sections coincide with the results of the so-called "fixed order plus next-to-leading log" approach of Refs. [192, 193]. The pure t and loop-induced tb-interference contributions have been separately reweighted with effective Higgs couplings, using an effective mixing angle α, and taking into account the resummation of $\tan\beta$-enhanced SUSY contributions as in the gluon fusion case. The same SM cross sections are also used to obtain the reweighted cross section for bbA production. A more detailed discussion is given in Ref. [84]. All Higgs boson masses, effective mixing angles, Yukawa couplings, branching fractions, and cross sections, and their uncertainties, which are taken into account for the exclusion contours, are obtained from Ref. [85].

In the figure, the exclusion sensitivity, estimated from the expected median in the absence of a signal, is indicated by the dashed black line. We note that the 68 and 95% central intervals, also given for the exclusion sensitivity, should not be misinterpreted as an uncertainty in the analysis, but they rather reflect the variation of the expected signal yield in the probed parameter space of the chosen benchmark scenarios. For the $M_{\mathrm{h,EFT}}^{125}$ scenario the sensitivity sharply drops at $m_{\mathrm{A}} = 2\,m_{\mathrm{t}}$, caused by a drop of the branching fractions of A and H into τ leptons where the A and H decays into two on-shell t quarks become kinematically accessible. The distinct boundary is related to the fact that in FEYNHIGGS, which is used for the calculation of all branching fractions for this benchmark scenario, only the decay into on-shell $\mathrm{t\bar{t}}$ pairs is implemented.

The parameter space of each benchmark scenario that is excluded at 95% CL by the data is indicated by the coloured blue area. Both scenarios are excluded at 95% CL for $m_{\mathrm{A}} \lesssim 350\,\mathrm{GeV}$. The local excess observed at 1.2 TeV, coupled with the comparably low signal of $\mu_{\mathrm{h}} = 0.82 \pm 0.11$ relative to the SM expectation for $\mathrm{h_{obs}}$, causes the deviation of the observed exclusion from the expectation. It should be noted that for large values of $\tan\beta$ the yield of $\mathrm{h_{obs}}$ still has a significant contribution to the sensitivity of the analysis in the m_{A}-$\tan\beta$ plane according to Ref. [85]. For $m_{\mathrm{A}} \lesssim 250\,\mathrm{GeV}$, most of the gg$\phi$ events do not enter the high-mass no b-tag categories due to the $m_{\tau\tau} \geq 250\,\mathrm{GeV}$ selection that is imposed to keep these categories orthogonal to the NN-categories. However, we still have some sensitivity to the ggϕ signal in these NN-categories, despite them being optimized for a SM-like signal at 125 GeV. Additionally, the yield of $\mathrm{h_{obs}}$ has a significant contribution to the sensitivity in this region, while the bbϕ signal in the b-tag categories increasingly contributes to the sensitivity for larger values of $\tan\beta$.

9 Summary

Three searches have been presented for signatures of physics beyond the standard model (SM) in $\tau\tau$ final states in proton-proton collisions at the LHC. The searches use a sample of proton-proton collisions collected with the CMS detector at a centre-of-mass energy of $\sqrt{s} = 13\,\mathrm{TeV}$, corresponding to an integrated luminosity of $138\,\mathrm{fb}^{-1}$. The data have been analysed in three different interpretations: in the context of a model-independent search for a (pseudo-)scalar resonance ϕ in addition to the observed Higgs boson, 95% confidence level (CL) upper limits have been set on the product of the branching fraction for the decay into τ leptons and the cross section for the production via gluon fusion or in association with b quarks, spanning four orders of magnitude from $\mathcal{O}(10\,\mathrm{pb})$ (for a mass of m_{ϕ} =60 GeV) to 0.3 fb (for m_{ϕ} =3.5 TeV) each. In the context of a search for non-resonant t-channel exchange of a vector leptoquark $\mathrm{U_1}$, 95% CL upper limits have been set on the coupling g_{U} ranging from 1 (for a mass of m_{U} =1 TeV) to 6 (for m_{U} =5 TeV), depending on the considered scenario. In the interpretation of benchmark scenarios of the minimal supersymmetric SM (MSSM), additional Higgs bosons with masses below 350 GeV are excluded at 95% CL. Depending on the scenario, the sensitivity of the data to exclude values of the MSSM parameter $\tan\beta$ reaches up to 1.8 TeV. The data reveal two excesses for ϕ production via gluon fusion with local p-values equivalent to approximately

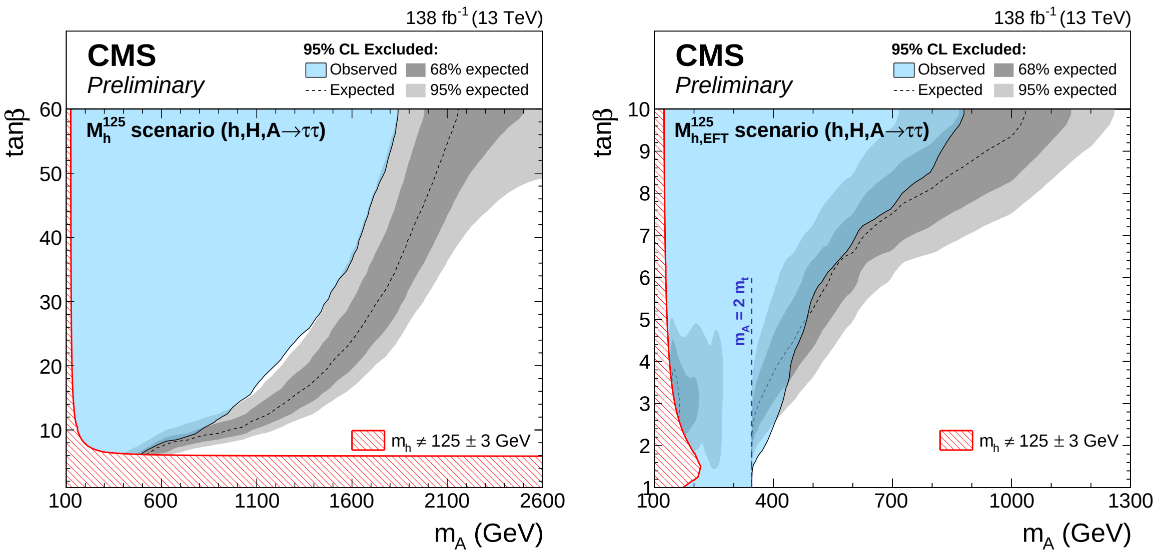

Figure 12: Expected 95% CL exclusion contours in the MSSM (left) M_{h}^{125} and (right) $M_{\mathrm{h,EFT}}^{125}$ scenarios. The expected median in the absence of a signal is shown as a dashed black line. The dark and bright grey bands indicate the associated 68 and 95% intervals of the expected exclusion. The observed exclusion contour is indicated by the coloured blue area. For both scenarios, those parts of the parameter space where m_{h} deviates by more then $\pm 3\,\mathrm{GeV}$ from the mass of $\mathrm{h}_{\mathrm{obs}}$ are indicated by a red hatched area. For the $M_{\mathrm{h,EFT}}^{125}$ scenario, the dashed blue line indicates the $m_{\mathrm{A}} = 2m_{\mathrm{t}}$ threshold whereby the $\mathrm{A} \to \mathrm{t\bar{t}}$ decay starts to influence the $\mathrm{A} \to \tau\tau$ branching fraction. The $\mathrm{H} \to \tau\tau$ branching fraction is influenced somewhat more gradually close to this threshold since the A and H are not completely degenerate in mass.

three s.d. at 100 GeV and 1.2 TeV, which are found to be consistent across $\tau\tau$ final states and data-taking years.

References

[1] ATLAS Collaboration, "Observation of a new particle in the search for the standard model Higgs boson with the ATLAS detector at the LHC", *Phys. Lett. B* **716** (2012) 1, doi:10.1016/j.physletb.2012.08.020, arXiv:1207.7214.

[2] CMS Collaboration, "Observation of a new boson at a mass of 125 GeV with the CMS experiment at the LHC", *Phys. Lett. B* **716** (2012) 30, doi:10.1016/j.physletb.2012.08.021, arXiv:1207.7235.

[3] CMS Collaboration, "Observation of a new boson with mass near 125 GeV in pp collisions at $\sqrt{s} = 7$ and 8 TeV", *JHEP* **06** (2013) 081, doi:10.1007/JHEP06(2013)081, arXiv:1303.4571.

[4] CMS Collaboration, "A measurement of the Higgs boson mass in the diphoton decay channel", *Phys. Lett. B* **805** (2020) 135425, doi:10.1016/j.physletb.2020.135425, arXiv:2002.06398.

[5] ATLAS and CMS Collaborations, "Measurements of the Higgs boson production and decay rates and constraints on its couplings from a combined ATLAS and CMS analysis of the LHC pp collision data at $\sqrt{s} = 7$ and 8 TeV", *JHEP* **08** (2016) 045, doi:10.1007/JHEP08(2016)045, arXiv:1606.02266.

[6] CMS Collaboration, "Combined measurements of Higgs boson couplings in proton–proton collisions at $\sqrt{s} = 13$ TeV", *Eur. Phys. J. C* **79** (2019) 421, doi:10.1140/epjc/s10052-019-6909-y, arXiv:1809.10733.

[7] ATLAS Collaboration, "Combined measurements of Higgs boson production and decay using up to 80 fb^{-1} of proton-proton collision data at $\sqrt{s} = 13$ TeV collected with the ATLAS experiment", *Phys. Rev. D* **101** (2020) 012002, doi:10.1103/PhysRevD.101.012002, arXiv:1909.02845.

[8] CMS Collaboration, "Measurements of the Higgs boson width and anomalous HVV couplings from on-shell and off-shell production in the four-lepton final state", *Phys. Rev. D* **99** (2019) 112003, doi:10.1103/PhysRevD.99.112003, arXiv:1901.00174.

[9] Yu. A. Golfand and E. P. Likhtman, "Extension of the algebra of Poincaré group generators and violation of p invariance", *JETP Lett.* **13** (1971) 323.

[10] J. Wess and B. Zumino, "Supergauge transformations in four dimensions", *Nucl. Phys. B* **70** (1974) 39, doi:10.1016/0550-3213(74)90355-1.

[11] P. Fayet, "Supergauge invariant extension of the Higgs mechanism and a model for the electron and its neutrino", *Nucl. Phys. B* **90** (1975) 104, doi:10.1016/0550-3213(75)90636-7.

[12] P. Fayet, "Spontaneously broken supersymmetric theories of weak, electromagnetic and strong interactions", *Phys. Lett. B* **69** (1977) 489, doi:10.1016/0370-2693(77)90852-8.

[13] DELPHI, OPAL, ALEPH, L3 and LEP Working Group for Higgs Boson Searches Collaboration, "Search for neutral MSSM Higgs bosons at LEP", *Eur. Phys. J. C* **47** (2006) 547, doi:10.1140/epjc/s2006-02569-7, arXiv:hep-ex/0602042.

[14] CDF Collaboration, “Search for Higgs bosons predicted in Two-Higgs-Doublet models via decays to tau lepton pairs in 1.96 TeV $p\bar{p}$ collisions”, *Phys. Rev. Lett.* **103** (2009) 201801, doi:10.1103/PhysRevLett.103.201801, arXiv:0906.1014.

[15] D0 Collaboration, “Search for neutral Higgs bosons in the multi-b-jet topology in 5.2 fb^{-1} of $p\bar{p}$ collisions at $\sqrt{s} = 1.96$ TeV”, *Phys. Lett. B* **698** (2011) 97, doi:10.1016/j.physletb.2011.02.062, arXiv:1011.1931.

[16] D0 Collaboration, “Search for Higgs bosons decaying to $\tau^+\tau^-$ pairs in $p\bar{p}$ collisions at $\sqrt{s} = 1.96$ TeV”, *Phys. Lett. B* **707** (2012) 323, doi:10.1016/j.physletb.2011.12.050, arXiv:1106.4555.

[17] CDF Collaboration, “Search for Higgs bosons produced in association with b-quarks”, *Phys. Rev. D* **85** (2012) 032005, doi:10.1103/PhysRevD.85.032005, arXiv:1106.4782.

[18] CMS Collaboration, “Search for a Higgs boson decaying into a b-quark pair and produced in association with b quarks in proton-proton collisions at 7 TeV”, *Phys. Lett. B* **722** (2013) 207, doi:10.1016/j.physletb.2013.04.017, arXiv:1302.2892.

[19] CMS Collaboration, “Search for neutral MSSM Higgs bosons decaying into a pair of bottom quarks”, *JHEP* **11** (2015) 071, doi:10.1007/JHEP11(2015)071, arXiv:1506.08329.

[20] CMS Collaboration, “Search for beyond the standard model Higgs bosons decaying into a $b\bar{b}$ pair in pp collisions at $\sqrt{s} = 13$ Tev”, *JHEP* **08** (2018) 113, doi:10.1007/JHEP08(2018)113, arXiv:1805.12191.

[21] ATLAS Collaboration, “Search for heavy neutral Higgs bosons produced in association with b-quarks and decaying into b-quarks at $\sqrt{s} = 13$ TeV with the ATLAS detector”, *Phys. Rev. D* **102** (2020) 032004, doi:10.1103/PhysRevD.102.032004, arXiv:1907.02749.

[22] ATLAS Collaboration, “Search for the neutral Higgs bosons of the minimal supersymmetric standard model in pp collisions at $\sqrt{s} = 7$ TeV with the ATLAS detector”, *JHEP* **02** (2013) 095, doi:10.1007/JHEP02(2013)095, arXiv:1211.6956.

[23] CMS Collaboration, “Search for neutral MSSM Higgs bosons decaying to $\mu^+\mu^-$ in pp collisions at $\sqrt{s} = 7$ and 8 TeV”, *Phys. Lett. B* **752** (2016) 221, doi:10.1016/j.physletb.2015.11.042, arXiv:1508.01437.

[24] CMS Collaboration, “Search for MSSM higgs bosons decaying to $\mu + \mu -$ in proton-proton collisions at $\sqrt{s} = 13$ TeV”, *Phys. Lett. B* **798** (2019) 134992, doi:10.1016/j.physletb.2019.134992, arXiv:1907.03152.

[25] ATLAS Collaboration, “Search for scalar resonances decaying into $\mu^+\mu^-$ in events with and without b-tagged jets produced in proton-proton collisions at $\sqrt{s} = 13$ TeV with the ATLAS detector”, *JHEP* **07** (2019) 117, doi:10.1007/JHEP07(2019)117, arXiv:1901.08144.

[26] ATLAS Collaboration, “Search for neutral Higgs bosons of the minimal supersymmetric standard model in pp collisions at $\sqrt{s} = 8$ TeV with the ATLAS detector”, *JHEP* **11** (2014) 056, doi:10.1007/JHEP11(2014)056, arXiv:1409.6064.

[27] ATLAS Collaboration, "Search for minimal supersymmetric standard model Higgs bosons H/A and for a Z′ boson in the $\tau\tau$ final state produced in pp collisions at $\sqrt{s} = 13$ TeV with the ATLAS detector", *Eur. Phys. J. C* **76** (2016) 585, doi:10.1140/epjc/s10052-016-4400-6, arXiv:1608.00890.

[28] ATLAS Collaboration, "Search for additional heavy neutral Higgs and gauge bosons in the ditau final state produced in 36 fb^{-1} of pp collisions at $\sqrt{s} = 13$ TeV with the ATLAS detector", *JHEP* **01** (2018) 055, doi:10.1007/JHEP01(2018)055, arXiv:1709.07242.

[29] CMS Collaboration, "Search for neutral minimal supersymmetric standard model Higgs bosons decaying to tau pairs in pp collisions at $\sqrt{s} = 7$ TeV", *Phys. Rev. Lett.* **106** (2011) 231801, doi:10.1103/PhysRevLett.106.231801, arXiv:1104.1619.

[30] CMS Collaboration, "Search for neutral Higgs bosons decaying to tau pairs in pp collisions at $\sqrt{s} = 7$ TeV", *Phys. Lett. B* **713** (2012) 68, doi:10.1016/j.physletb.2012.05.028, arXiv:1202.4083.

[31] CMS Collaboration, "Search for neutral MSSM Higgs bosons decaying to a pair of tau leptons in pp collisions", *JHEP* **10** (2014) 160, doi:10.1007/JHEP10(2014)160, arXiv:1408.3316.

[32] CMS Collaboration, "Search for additional neutral MSSM higgs bosons in the $\tau\tau$ final state in proton-proton collisions at $\sqrt{s} = 13$ TeV", *JHEP* **09** (2018) 007, doi:10.1007/JHEP09(2018)007, arXiv:1803.06553.

[33] ATLAS Collaboration, "Search for heavy Higgs bosons decaying into two tau leptons with the ATLAS detector using pp collisions at $\sqrt{s} = 13$ TeV", *Phys. Rev. Lett.* **125** (2020) 051801, doi:10.1103/PhysRevLett.125.051801, arXiv:2002.12223.

[34] J. Steggemann, "Extended scalar sectors", *Ann. Rev. Nucl. Part. Sci.* **70** (2020) 197, doi:10.1146/annurev-nucl-032620-043846.

[35] B. Diaz, M. Schmaltz, and Y.-M. Zhong, "The leptoquark hunter's guide: Pair production", *JHEP* **10** (2017) 097, doi:10.1007/JHEP10(2017)097, arXiv:1706.05033.

[36] M. Schmaltz and Y.-M. Zhong, "The leptoquark hunter's guide: Large coupling", *JHEP* **01** (2019) 132, doi:10.1007/JHEP01(2019)132, arXiv:1810.10017.

[37] CMS Collaboration, "Search for third-generation scalar leptoquarks and heavy right-handed neutrinos in final states with two tau leptons and two jets in proton-proton collisions at $\sqrt{s} = 13$ TeV", *JHEP* **07** (2017) 121, doi:10.1007/JHEP07(2017)121, arXiv:1703.03995.

[38] CMS Collaboration, "Search for a singly produced third-generation scalar leptoquark decaying to a τ lepton and a bottom quark in proton-proton collisions at $\sqrt{s} = 13$ TeV", *JHEP* **07** (2018) 115, doi:10.1007/JHEP07(2018)115, arXiv:1806.03472.

[39] CMS Collaboration, "Search for heavy neutrinos and third-generation leptoquarks in hadronic states of two τ leptons and two jets in proton-proton collisions at $\sqrt{s} = 13$ TeV", *JHEP* **03** (2019) 170, doi:10.1007/JHEP03(2019)170, arXiv:1811.00806.

[40] ATLAS Collaboration, "Searches for third-generation scalar leptoquarks in $\sqrt{s}$ = 13 TeV pp collisions with the ATLAS detector", *JHEP* **06** (2019) 144, doi:10.1007/JHEP06(2019)144, arXiv:1902.08103.

[41] ATLAS Collaboration, "Search for a scalar partner of the top quark in the all-hadronic $t\bar{t}$ plus missing transverse momentum final state at $\sqrt{s} = 13$ TeV with the ATLAS detector", *Eur. Phys. J. C* **80** (2020) 737, doi:10.1140/epjc/s10052-020-8102-8, arXiv:2004.14060.

[42] CMS Collaboration, "Search for singly and pair-produced leptoquarks coupling to third-generation fermions in proton-proton collisions at s=13 TeV", *Phys. Lett. B* **819** (2021) 136446, doi:10.1016/j.physletb.2021.136446, arXiv:2012.04178.

[43] ATLAS Collaboration, "Search for new phenomena in pp collisions in final states with tau leptons, b-jets, and missing transverse momentum with the ATLAS detector", *Phys. Rev. D* **104** (2021) 112005, doi:10.1103/PhysRevD.104.112005, arXiv:2108.07665.

[44] ATLAS Collaboration, "Search for new phenomena in final states with b-jets and missing transverse momentum in $\sqrt{s} = 13$ TeV pp collisions with the ATLAS detector", *JHEP* **05** (2021) 093, doi:10.1007/JHEP05(2021)093, arXiv:2101.12527.

[45] ATLAS Collaboration, "Search for pair production of third-generation scalar leptoquarks decaying into a top quark and a τ-lepton in pp collisions at $\sqrt{s}$ = 13 TeV with the ATLAS detector", *JHEP* **06** (2021) 179, doi:10.1007/JHEP06(2021)179, arXiv:2101.11582.

[46] J. C. Pati and A. Salam, "Unified lepton-hadron symmetry and a gauge theory of the basic interactions", *Phys. Rev. D* **8** (1973) 1240, doi:10.1103/PhysRevD.8.1240.

[47] J. C. Pati and A. Salam, "Lepton number as the fourth color", *Phys. Rev. D* **10** (1974) 275, doi:10.1103/PhysRevD.10.275. [Erratum: doi:10.1103/PhysRevD.11.703.2].

[48] H. Georgi and S. L. Glashow, "Unity of all elementary particle forces", *Phys. Rev. Lett.* **32** (1974) 438, doi:10.1103/PhysRevLett.32.438.

[49] H. Fritzsch and P. Minkowski, "Unified interactions of leptons and hadrons", *Ann. Phys.* **93** (1975) 193, doi:10.1016/0003-4916(75)90211-0.

[50] S. Dimopoulos and L. Susskind, "Mass without scalars", *Nucl. Phys. B* **155** (1979) 237, doi:10.1016/0550-3213(79)90364-X.

[51] S. Dimopoulos, "Technicolored signatures", *Nucl. Phys. B* **168** (1980) 69, doi:10.1016/0550-3213(80)90277-1.

[52] E. Farhi and L. Susskind, "Technicolor", *Phys. Rept.* **74** (1981) 277, doi:10.1016/0370-1573(81)90173-3.

[53] K. D. Lane and M. V. Ramana, "Walking technicolor signatures at hadron colliders", *Phys. Rev. D* **44** (1991) 2678, doi:10.1103/PhysRevD.44.2678.

[54] B. Schrempp and F. Schrempp, "Light leptoquarks", *Phys. Lett. B* **153** (1985) 101, doi:10.1016/0370-2693(85)91450-9.

[55] B. Gripaios, "Composite leptoquarks at the LHC", *JHEP* **02** (2010) 045, doi:10.1007/JHEP02(2010)045, arXiv:0910.1789.

[56] G. R. Farrar and P. Fayet, "Phenomenology of the production, decay, and detection of new hadronic states associated with supersymmetry", *Phys. Lett. B* **76** (1978) 575, doi:10.1016/0370-2693(78)90858-4.

[57] P. Ramond, "Dual theory for free fermions", *Phys. Rev. D* **3** (1971) 2415, doi:10.1103/PhysRevD.3.2415.

[58] A. Neveu and J. H. Schwarz, "Factorizable dual model of pions", *Nucl. Phys. B* **31** (1971) 86, doi:10.1016/0550-3213(71)90448-2.

[59] D. V. Volkov and V. P. Akulov, "Possible universal neutrino interaction", *JETP Lett.* **16** (1972) 438.

[60] J. Wess and B. Zumino, "A Lagrangian model invariant under supergauge transformations", *Phys. Lett. B* **49** (1974) 52, doi:10.1016/0370-2693(74)90578-4.

[61] H. P. Nilles, "Supersymmetry, supergravity and particle physics", *Phys. Rept.* **110** (1984) 1, doi:10.1016/0370-1573(84)90008-5.

[62] R. Barbier et al., "R-parity violating supersymmetry", *Phys. Rept.* **420** (2005) 1, doi:10.1016/j.physrep.2005.08.006, arXiv:hep-ph/0406039.

[63] M. Tanaka and R. Watanabe, "New physics in the weak interaction of $\bar{B} \to D^{(*)}\tau\bar{\nu}$", *Phys. Rev. D* **87** (2013) 034028, doi:10.1103/PhysRevD.87.034028, arXiv:1212.1878.

[64] R. Barbieri, G. Isidori, A. Pattori, and F. Senia, "Anomalies in B-decays and $U(2)$ flavour symmetry", *Eur. Phys. J. C* **76** (2016) 67, doi:10.1140/epjc/s10052-016-3905-3, arXiv:1512.01560.

[65] D. A. Faroughy, A. Greljo, and J. F. Kamenik, "Confronting lepton flavor universality violation in B decays with high-p_{T} tau lepton searches at LHC", *Phys. Lett. B* **764** (2017) 126, doi:10.1016/j.physletb.2016.11.011, arXiv:1609.07138.

[66] M. Bordone, C. Cornella, J. Fuentes-Martin, and G. Isidori, "A three-site gauge model for flavor hierarchies and flavor anomalies", *Phys. Lett. B* **779** (2018) 317, doi:10.1016/j.physletb.2018.02.011, arXiv:1712.01368.

[67] L. Di Luzio, A. Greljo, and M. Nardecchia, "Gauge leptoquark as the origin of B-physics anomalies", *Phys. Rev. D* **96** (2017) 115011, doi:10.1103/PhysRevD.96.115011, arXiv:1708.08450.

[68] A. Greljo and B. A. Stefanek, "Third family quark–lepton unification at the TeV scale", *Phys. Lett. B* **782** (2018) 131, doi:10.1016/j.physletb.2018.05.033, arXiv:1802.04274.

[69] A. Angelescu et al., "Single leptoquark solutions to the B-physics anomalies", *Phys. Rev. D* **104** (2021) 055017, doi:10.1103/PhysRevD.104.055017, arXiv:2103.12504.

[70] C. Cornella et al., "Reading the footprints of the B-meson flavor anomalies", *JHEP* **08** (2021) 050, doi:10.1007/JHEP08(2021)050, arXiv:2103.16558.

[71] LHCb Collaboration, "Test of lepton universality in beauty-quark decays", 2021. arXiv:2103.11769. Submitted to *Nat. Phys.*

[72] BaBar Collaboration, "Evidence for an excess of $\bar{B} \to D^{(*)}\tau^-\bar{\nu}_\tau$ decays", *Phys. Rev. Lett.* **109** (2012) 101802, doi:10.1103/PhysRevLett.109.101802, arXiv:1205.5442.

[73] BaBar Collaboration, "Measurement of an excess of $\bar{B} \to D^{(*)}\tau^-\bar{\nu}_\tau$ decays and implications for charged higgs bosons", *Phys. Rev. D* **88** (2013) 072012, doi:10.1103/PhysRevD.88.072012, arXiv:1303.0571.

[74] Belle Collaboration, "Measurement of the branching ratio of $\bar{B} \to D^{(*)}\tau^-\bar{\nu}_\tau$ relative to $\bar{B} \to D^{(*)}\ell^-\bar{\nu}_\ell$ decays with hadronic tagging at Belle", *Phys. Rev. D* **92** (2015) 072014, doi:10.1103/PhysRevD.92.072014, arXiv:1507.03233.

[75] LHCb Collaboration, "Measurement of the ratio of branching fractions $\mathcal{B}(\bar{B}^0 \to D^{*+}\tau^-\bar{\nu}_\tau)/\mathcal{B}(\bar{B}^0 \to D^{*+}\mu^-\bar{\nu}_\mu)$", *Phys. Rev. Lett.* **115** (2015) 111803, doi:10.1103/PhysRevLett.115.111803, arXiv:1506.08614. [Erratum: doi:10.1103/PhysRevLett.115.159901].

[76] Belle Collaboration, "Measurement of the τ lepton polarization and $R(D^*)$ in the decay $\bar{B} \to D^*\tau^-\bar{\nu}_\tau$", *Phys. Rev. Lett.* **118** (2017) 211801, doi:10.1103/PhysRevLett.118.211801, arXiv:1612.00529.

[77] LHCb Collaboration, "Test of lepton flavor universality by the measurement of the $B^0 \to D^{*-}\tau^+\nu_\tau$ branching fraction using three-prong τ decays", *Phys. Rev. D* **97** (2018) 072013, doi:10.1103/PhysRevD.97.072013, arXiv:1711.02505.

[78] LHCb Collaboration, "Measurement of the ratio of the $B^0 \to D^{*-}\tau^+\nu_\tau$ and $B^0 \to D^{*-}\mu^+\nu_\mu$ branching fractions using three-prong τ-lepton decays", *Phys. Rev. Lett.* **120** (2018) 171802, doi:10.1103/PhysRevLett.120.171802, arXiv:1708.08856.

[79] T. D. Lee, "A theory of spontaneous T violation", *Phys. Rev. D* (1973) 1226, doi:10.1103/PhysRevD.8.1226.

[80] G. C. Branco et al., "Theory and phenomenology of two-Higgs-doublet models", *Phys. Rept.* (2012) 1, doi:10.1016/j.physrep.2012.02.002, arXiv:1106.0034.

[81] E. Bagnaschi et al., "MSSM Higgs boson searches at the LHC: Benchmark scenarios for Run 2 and beyond", *Eur. Phys. J. C* **79** (2019) 617, doi:10.1140/epjc/s10052-019-7114-8, arXiv:1808.07542.

[82] H. Bahl et al., "HL-LHC and ILC sensitivities in the hunt for heavy Higgs bosons", *Eur. Phys. J. C* **80** (2020) 916, doi:10.1140/epjc/s10052-020-08472-z, arXiv:2005.14536.

[83] H. Bahl, S. Liebler, and T. Stefaniak, "MSSM Higgs benchmark scenarios for Run 2 and beyond: the low $\tan\beta$ region", *Eur. Phys. J. C* **79** (2019) 279, doi:10.1140/epjc/s10052-019-6770-z, arXiv:1901.05933.

[84] E. A. Bagnaschi et al., "Benchmark scenarios for MSSM Higgs boson searches at the LHC", technical report, CERN, Geneva, 2021.

[85] LHC Higgs Cross Section Working Group – MSSM subgroup, "LHCHWG MSSM ROOT files", 2022. doi:10.5281/zenodo.6334713.

[86] CMS Collaboration, "Performance of the CMS Level-1 trigger in proton-proton collisions at $\sqrt{s} = 13$ TeV", *JINST* **15** (2020) P10017, doi:10.1088/1748-0221/15/10/P10017, arXiv:2006.10165.

[87] CMS Collaboration, "The CMS trigger system", *JINST* **12** (2017) P01020, doi:10.1088/1748-0221/12/01/P01020, arXiv:1609.02366.

[88] CMS Collaboration, "The CMS experiment at the CERN LHC", *JINST* **3** (2008) S08004, doi:10.1088/1748-0221/3/08/S08004.

[89] CMS Collaboration, "Particle-flow reconstruction and global event description with the CMS detector", *JINST* **12** (2017) P10003, doi:10.1088/1748-0221/12/10/P10003, arXiv:1706.04965.

[90] M. Cacciari, G. P. Salam, and G. Soyez, "FastJet user manual", *Eur. Phys. J. C* **72** (2012) 1896, doi:10.1140/epjc/s10052-012-1896-2, arXiv:1111.6097.

[91] CMS Collaboration, "Performance of electron reconstruction and selection with the CMS detector in proton-proton collisions at $\sqrt{s} = 8$ TeV", *JINST* **10** (2015) P06005, doi:10.1088/1748-0221/10/06/P06005, arXiv:1502.02701.

[92] CMS Collaboration, "Electron and photon reconstruction and identification with the CMS experiment at the CERN LHC", 2020. arXiv:2012.06888. Submitted to *JINST*.

[93] CMS Collaboration, "Performance of the CMS muon detector and muon reconstruction with proton-proton collisions at $\sqrt{s} = 13$ TeV", *JINST* **13** (2018) P06015, doi:10.1088/1748-0221/13/06/P06015, arXiv:1804.04528.

[94] CMS Collaboration, "Identification of heavy-flavour jets with the CMS detector in pp collisions at 13 TeV", *JINST* **13** (2018) P05011, doi:10.1088/1748-0221/13/05/P05011, arXiv:1712.07158.

[95] E. Bols et al., "Jet flavour classification using DeepJet", *JINST* **15** (2020) P12012, doi:10.1088/1748-0221/15/12/P12012, arXiv:2008.10519.

[96] CMS Collaboration, "Performance of the DeepJet b tagging algorithm using 41.9/fb of data from proton-proton collisions at 13 TeV with Phase 1 CMS detector", CMS Detector Performance Note CMS-DP-2018-058, 2018.

[97] CMS Collaboration, "Performance of reconstruction and identification of τ leptons decaying to hadrons and ν_τ in pp collisions at $\sqrt{s} = 13$ TeV", *JINST* **13** (2018) P10005, doi:10.1088/1748-0221/13/10/P10005, arXiv:1809.02816.

[98] CMS Collaboration, "Identification of hadronic tau lepton decays using a deep neural network", 2022. arXiv:2201.08458. Submitted to *JINST*.

[99] CMS Collaboration, "Performance of missing transverse momentum reconstruction in proton-proton collisions at $\sqrt{s} = 13$ TeV using the CMS detector", *JINST* **14** (2019) P07004, doi:10.1088/1748-0221/14/07/P07004, arXiv:1903.06078.

[100] D. Bertolini, P. Harris, M. Low, and N. Tran, "Pileup per particle identification", *JHEP* **10** (2014) 059, doi:10.1007/JHEP10(2014)059, arXiv:1407.6013.

[101] CDF Collaboration, "Search for neutral Higgs bosons of the minimal supersymmetric standard model decaying to τ pairs in $p\bar{p}$ collisions at $\sqrt{s} = 1.96$ TeV", *Phys. Rev. Lett.* **96** (2006) 011802, doi:10.1103/PhysRevLett.96.011802, arXiv:hep-ex/0508051.

[102] L. Bianchini, J. Conway, E. K. Friis, and C. Veelken, "Reconstruction of the Higgs mass in $H \to \tau\tau$ events by dynamical likelihood techniques", *J. Phys. Conf. Ser.* **513** (2014) 022035, doi:10.1088/1742-6596/513/2/022035.

[103] B. K. Bullock, K. Hagiwara, and A. D. Martin, "Tau polarization and its correlations as a probe of new physics", *Nucl. Phys. B* **395** (1993) 499, doi:10.1016/0550-3213(93)90045-Q.

[104] Particle Data Group Collaboration, "Review of particle physics", *PTEP* **2020** (2020) 083C01, doi:10.1093/ptep/ptaa104.

[105] CMS Collaboration, "Measurement of Higgs boson production and decay to the $\tau\tau$ final state", CMS Physics Analysis Summary CMS-PAS-HIG-18-032, 2019.

[106] CMS Collaboration, "An embedding technique to determine $\tau\tau$ backgrounds in proton-proton collision data", *JINST* **14** (2019) P06032, doi:10.1088/1748-0221/14/06/P06032, arXiv:1903.01216.

[107] CMS Collaboration, "Measurement of the $Z/\gamma^* \to \tau\tau$ cross section in pp collisions at $\sqrt{s} = 13$ TeV and validation of τ lepton analysis techniques", *Eur. Phys. J. C* **78** (2018) 708, doi:10.1140/epjc/s10052-018-6146-9, arXiv:1801.03535.

[108] J. Alwall et al., "MadGraph 5: Going beyond", *JHEP* **06** (2011) 128, doi:10.1007/JHEP06(2011)128, arXiv:1106.0522.

[109] J. Alwall et al., "The automated computation of tree-level and next-to-leading order differential cross sections, and their matching to parton shower simulations", *JHEP* **07** (2014) 079, doi:10.1007/JHEP07(2014)079, arXiv:1405.0301.

[110] R. Frederix and S. Frixione, "Merging meets matching in MC@NLO", *JHEP* **12** (2012) 061, doi:10.1007/JHEP12(2012)061, arXiv:1209.6215.

[111] J. Alwall et al., "Comparative study of various algorithms for the merging of parton showers and matrix elements in hadronic collisions", *Eur. Phys. J. C* **53** (2008) 473, doi:10.1140/epjc/s10052-007-0490-5, arXiv:0706.2569.

[112] S. Alioli, S.-O. Moch, and P. Uwer, "Hadronic top-quark pair-production with one jet and parton showering", *JHEP* **01** (2012) 137, doi:10.1007/JHEP01(2012)137, arXiv:1110.5251.

[113] R. Frederix, E. Re, and P. Torrielli, "Single-top t-channel hadroproduction in the four-flavour scheme with POWHEG and aMC@NLO", *JHEP* **09** (2012) 130, doi:10.1007/JHEP09(2012)130, arXiv:1207.5391.

[114] P. Nason, "A new method for combining NLO QCD with shower Monte Carlo algorithms", *JHEP* **11** (2004) 040, doi:10.1088/1126-6708/2004/11/040, arXiv:hep-ph/0409146.

[115] S. Frixione, P. Nason, and C. Oleari, "Matching NLO QCD computations with parton shower simulations: the POWHEG method", *JHEP* **11** (2007) 070, doi:10.1088/1126-6708/2007/11/070, arXiv:0709.2092.

[116] S. Alioli, P. Nason, C. Oleari, and E. Re, "A general framework for implementing NLO calculations in shower Monte Carlo programs: the POWHEG BOX", *JHEP* **06** (2010) 043, doi:10.1007/JHEP06(2010)043, arXiv:1002.2581.

[117] T. Ježo and P. Nason, "On the treatment of resonances in next-to-leading order calculations matched to a parton shower", *JHEP* **12** (2015) 065, doi:10.1007/JHEP12(2015)065, arXiv:1509.09071.

[118] E. Re, "Single-top Wt-channel production matched with parton showers using the POWHEG method", *Eur. Phys. J. C* **71** (2011) 1547, doi:10.1140/epjc/s10052-011-1547-z, arXiv:1009.2450.

[119] K. Melnikov and F. Petriello, "Electroweak gauge boson production at hadron colliders through $\mathcal{O}(\alpha_s^2)$", *Phys. Rev. D* **74** (2006) 114017, doi:10.1103/PhysRevD.74.114017, arXiv:hep-ph/0609070.

[120] M. Czakon and A. Mitov, "Top++: A program for the calculation of the top-pair cross-section at hadron colliders", *Comput. Phys. Commun.* **185** (2014) 2930, doi:10.1016/j.cpc.2014.06.021, arXiv:1112.5675.

[121] N. Kidonakis, "Top quark production", in *Proceedings, Helmholtz International Summer School on Physics of Heavy Quarks and Hadrons (HQ 2013): JINR, Dubna, Russia, July 15-28, 2013*, p. 139. 2014. arXiv:1311.0283. doi:10.3204/DESY-PROC-2013-03/Kidonakis.

[122] J. M. Campbell, R. K. Ellis, and C. Williams, "Vector boson pair production at the LHC", *JHEP* **07** (2011) 018, doi:10.1007/JHEP07(2011)018, arXiv:1105.0020.

[123] T. Gehrmann et al., "W^+W^- production at hadron colliders in next to next to leading order QCD", *Phys. Rev. Lett.* **113** (2014) 212001, doi:10.1103/PhysRevLett.113.212001, arXiv:1408.5243.

[124] E. Bagnaschi, G. Degrassi, P. Slavich, and A. Vicini, "Higgs production via gluon fusion in the POWHEG approach in the SM and in the MSSM", *JHEP* **02** (2012) 088, doi:10.1007/JHEP02(2012)088, arXiv:1111.2854.

[125] P. Nason and C. Oleari, "NLO Higgs boson production via vector-boson fusion matched with shower in POWHEG", *JHEP* **02** (2010) 037, doi:10.1007/JHEP02(2010)037, arXiv:0911.5299.

[126] G. Luisoni, P. Nason, C. Oleari, and F. Tramontano, "$HW^{\pm}$/HZ + 0 and 1 jet at NLO with the POWHEG BOX interfaced to GoSam and their merging within MiNLO", *JHEP* **10** (2013) 083, doi:10.1007/JHEP10(2013)083, arXiv:1306.2542.

[127] F. Granata, J. M. Lindert, C. Oleari, and S. Pozzorini, "NLO QCD+EW predictions for HV and HV+jet production including parton-shower effects", *JHEP* **09** (2017) 012, doi:10.1007/JHEP09(2017)012, arXiv:1706.03522.

[128] K. Hamilton, P. Nason, E. Re, and G. Zanderighi, "NNLOPS simulation of Higgs boson production", *JHEP* **10** (2013) 222, doi:10.1007/JHEP10(2013)222, arXiv:1309.0017.

[129] K. Hamilton, P. Nason, and G. Zanderighi, "Finite quark-mass effects in the NNLOPS POWHEG+MiNLO Higgs generator", *JHEP* **05** (2015) 140, doi:10.1007/JHEP05(2015)140, arXiv:1501.04637.

[130] R. V. Harlander, H. Mantler, and M. Wiesemann, "Transverse momentum resummation for Higgs production via gluon fusion in the MSSM", *JHEP* **11** (2014) 116, doi:10.1007/JHEP11(2014)116, arXiv:1409.0531.

[131] E. Bagnaschi et al., "Resummation ambiguities in the Higgs transverse-momentum spectrum in the standard model and beyond", *JHEP* **01** (2016) 090, doi:10.1007/JHEP01(2016)090, arXiv:1510.08850.

[132] E. Bagnaschi and A. Vicini, "The Higgs transverse momentum distribution in gluon fusion as a multiscale problem", *JHEP* **01** (2016) 056, doi:10.1007/JHEP01(2016)056, arXiv:1505.00735.

[133] B. Jager, L. Reina, and D. Wackeroth, "Higgs boson production in association with b jets in the POWHEG BOX", *Phys. Rev. D* **93** (2016) 014030, doi:10.1103/PhysRevD.93.014030, arXiv:1509.05843.

[134] M. J. Baker, J. Fuentes-Martín, G. Isidori, and M. König, "High- p_{T} signatures in vector–leptoquark models", *Eur. Phys. J. C* **79** (2019) 334, doi:10.1140/epjc/s10052-019-6853-x, arXiv:1901.10480.

[135] J. Butterworth et al., "PDF4LHC recommendations for LHC Run II", *J. Phys. G* **43** (2016) 023001, doi:10.1088/0954-3899/43/2/023001, arXiv:1510.03865.

[136] NNPDF Collaboration, "Parton distributions from high-precision collider data", *Eur. Phys. J. C* **77** (2017) 663, doi:10.1140/epjc/s10052-017-5199-5, arXiv:1706.00428.

[137] NNPDF Collaboration, "Parton distributions for the LHC Run II", *JHEP* **04** (2015) 040, doi:10.1007/JHEP04(2015)040, arXiv:1410.8849.

[138] CMS Collaboration, "Event generator tunes obtained from underlying event and multiparton scattering measurements", *Eur. Phys. J. C* **76** (2016) 155, doi:10.1140/epjc/s10052-016-3988-x, arXiv:1512.00815.

[139] CMS Collaboration, "Extraction and validation of a new set of CMS PYTHIA8 tunes from underlying-event measurements", *Eur. Phys. J. C* **80** (2020) 4, doi:10.1140/epjc/s10052-019-7499-4, arXiv:1903.12179.

[140] T. Sjöstrand et al., "An introduction to PYTHIA 8.2", *Comput. Phys. Commun.* **191** (2015) 159, doi:10.1016/j.cpc.2015.01.024, arXiv:1410.3012.

[141] S. Agostinelli et al., "GEANT4—a simulation toolkit", *Nucl. Instrum. Meth. A* **506** (2003) 250, doi:10.1016/S0168-9002(03)01368-8.

[142] R. J. Barlow and C. Beeston, "Fitting using finite Monte Carlo samples", *Comput. Phys. Commun.* **77** (1993) 219, doi:10.1016/0010-4655(93)90005-W.

[143] J. S. Conway, "Incorporating nuisance parameters in likelihoods for multisource spectra", in *PHYSTAT 2011*, p. 115. 2011. arXiv:1103.0354. doi:10.5170/CERN-2011-006.115.

[144] CMS Collaboration, "Measurements of inclusive W and Z cross sections in pp collisions at $\sqrt{s} = 7\,\text{TeV}$", *JHEP* **01** (2011) 080, doi:10.1007/JHEP01(2011)080, arXiv:1012.2466.

[145] CMS Collaboration, "Measurement of the differential cross section for top quark pair production in pp collisions at $\sqrt{s} = 8\,\text{TeV}$", *Eur. Phys. J. C* **75** (2015) 542, doi:10.1140/epjc/s10052-015-3709-x, arXiv:1505.04480.

[146] CMS Collaboration, "Precision luminosity measurement in proton-proton collisions at $\sqrt{s} = 13\,\text{TeV}$ in 2015 and 2016 at CMS", *Eur. Phys. J. C* **81** (2021) 800, doi:10.1140/epjc/s10052-021-09538-2, arXiv:2104.01927.

[147] CMS Collaboration, "CMS luminosity measurement for the 2017 data taking period at $\sqrt{s} = 13\,\text{TeV}$", CMS Physics Analysis Summary CMS-PAS-LUM-17-004, 2018.

[148] CMS Collaboration, "CMS luminosity measurement for the 2018 data-taking period at $\sqrt{s} = 13\,\text{TeV}$", CMS Physics Analysis Summary CMS-PAS-LUM-18-002, 2019.

[149] LHC Higgs Cross Section Working Group, "Handbook of LHC Higgs cross sections: 4. deciphering the nature of the Higgs sector", technical report, CERN, 2016. doi:10.23731/CYRM-2017-002, arXiv:1610.07922.

[150] S. Alioli, P. Nason, C. Oleari, and E. Re, "NLO Higgs boson production via gluon fusion matched with shower in POWHEG", *JHEP* **04** (2009) 002, doi:10.1088/1126-6708/2009/04/002, arXiv:0812.0578.

[151] H. B. Hartanto, B. Jager, L. Reina, and D. Wackeroth, "Higgs boson production in association with top quarks in the POWHEG BOX", *Phys. Rev. D* **91** (2015) 094003, doi:10.1103/PhysRevD.91.094003, arXiv:1501.04498.

[152] ATLAS and CMS Collaborations, "Procedure for the LHC Higgs boson search combination in summer 2011", Technical Report ATL-PHYS-PUB 2011-11, CMS NOTE 2011/005, , 2011.

[153] CMS Collaboration, "Combined results of searches for the standard model Higgs boson in pp collisions at $\sqrt{s} = 7\,\text{TeV}$", *Phys. Lett. B* **710** (2012) 26, doi:10.1016/j.physletb.2012.02.064, arXiv:1202.1488.

[154] G. Cowan, K. Cranmer, E. Gross, and O. Vitells, "Asymptotic formulae for likelihood-based tests of new physics", *Eur. Phys. J. C* **71** (2011) 1554, doi:10.1140/epjc/s10052-011-1554-0, arXiv:1007.1727. [Erratum: doi:10.1140/epjc/s10052-013-2501-z].

[155] T. Junk, "Confidence level computation for combining searches with small statistics", *Nucl. Instrum. Meth. A* **434** (1999) 435, doi:10.1016/S0168-9002(99)00498-2, arXiv:hep-ex/9902006.

[156] A. L. Read, "Presentation of search results: The CL_s technique", *J. Phys. G* **28** (2002) 2693, doi:10.1088/0954-3899/28/10/313.

[157] CMS Collaboration, "Search for a standard model-like Higgs boson in the mass range between 70 and 110 GeV in the diphoton final state in proton-proton collisions at $\sqrt{s} = 8$ and 13 TeV", *Phys. Lett. B* (2019) 320, doi:10.1016/j.physletb.2019.03.064, arXiv:1811.08459.

[158] P. Slavich et al., "Higgs-mass predictions in the MSSM and beyond", *Eur. Phys. J. C* **81** (2021) 450, doi:10.1140/epjc/s10052-021-09198-2, arXiv:2012.15629.

[159] A. L. Read, "Linear interpolation of histograms", *Nucl. Instrum. Meth. A* **425** (1999) 357, doi:10.1016/S0168-9002(98)01347-3.

[160] S. Heinemeyer, W. Hollik, and G. Weiglein, "FeynHiggs: A program for the calculation of the masses of the neutral CP-even Higgs bosons in the MSSM", *Comput. Phys. Commun.* **124** (2000) 76, doi:10.1016/S0010-4655(99)00364-1, arXiv:hep-ph/9812320.

[161] S. Heinemeyer, W. Hollik, and G. Weiglein, "The masses of the neutral CP-even Higgs bosons in the MSSM: Accurate analysis at the two-loop level", *Eur. Phys. J. C* **9** (1999) 343, doi:10.1007/s100529900006, arXiv:hep-ph/9812472.

[162] G. Degrassi et al., "Towards high-precision predictions for the MSSM Higgs sector", *Eur. Phys. J. C* **28** (2003) 133, doi:10.1140/epjc/s2003-01152-2, arXiv:hep-ph/0212020.

[163] M. Frank et al., "The Higgs boson masses and mixings of the complex MSSM in the Feynman-diagrammatic approach", *JHEP* **02** (2007) 047, doi:10.1088/1126-6708/2007/02/047, arXiv:hep-ph/0611326.

[164] T. Hahn et al., "High-precision predictions for the light CP-even Higgs boson mass of the minimal supersymmetric standard model", *Phys. Rev. Lett.* **112** (2014) 141801, doi:10.1103/PhysRevLett.112.141801, arXiv:1312.4937.

[165] H. Bahl and W. Hollik, "Precise prediction for the light MSSM Higgs boson mass combining effective field theory and fixed-order calculations", *Eur. Phys. J. C* **76** (2016), no. 9, 499, doi:10.1140/epjc/s10052-016-4354-8, arXiv:1608.01880.

[166] H. Bahl, S. Heinemeyer, W. Hollik, and G. Weiglein, "Reconciling EFT and hybrid calculations of the light MSSM Higgs-boson mass", *Eur. Phys. J. C* **78** (2018), no. 1, 57, doi:10.1140/epjc/s10052-018-5544-3, arXiv:1706.00346.

[167] H. Bahl et al., "Precision calculations in the MSSM Higgs-boson sector with FeynHiggs 2.14", *Comput. Phys. Commun.* **249** (2020) 107099, doi:10.1016/j.cpc.2019.107099, arXiv:1811.09073.

[168] A. Djouadi, J. Kalinowski, and M. Spira, "HDECAY: A program for Higgs boson decays in the standard model and its supersymmetric extension", *Comput. Phys. Commun.* **108** (1998) 56, doi:10.1016/S0010-4655(97)00123-9, arXiv:hep-ph/9704448.

[169] A. Djouadi, J. Kalinowski, M. Muehlleitner, and M. Spira, "HDECAY: Twenty$_{++}$ years after", *Comput. Phys. Commun.* **238** (2019) 214, doi:10.1016/j.cpc.2018.12.010, arXiv:1801.09506.

[170] LHC Higgs Cross Section Working Group, "Handbook of LHC Higgs cross sections: 3. Higgs properties", technical report, CERN, 2013. doi:10.5170/CERN-2013-004, arXiv:1307.1347.

[171] A. Denner et al., "Standard model Higgs-boson branching ratios with uncertainties", *Eur. Phys. J. C* **71** (2011) 1753, doi:10.1140/epjc/s10052-011-1753-8, arXiv:1107.5909.

[172] R. V. Harlander, S. Liebler, and H. Mantler, "SusHi: A program for the calculation of Higgs production in gluon fusion and bottom-quark annihilation in the standard model and the MSSM", *Comput. Phys. Commun.* **184** (2013) 1605, doi:10.1016/j.cpc.2013.02.006, arXiv:1212.3249.

[173] R. V. Harlander, S. Liebler, and H. Mantler, "SusHi Bento: Beyond NNLO and the heavy-top limit", *Comput. Phys. Commun.* **212** (2017) 239, doi:10.1016/j.cpc.2016.10.015, arXiv:1605.03190.

[174] M. Spira, A. Djouadi, D. Graudenz, and P. M. Zerwas, "Higgs boson production at the LHC", *Nucl. Phys. B* **453** (1995) 17, doi:10.1016/0550-3213(95)00379-7, arXiv:hep-ph/9504378.

[175] R. Harlander and P. Kant, "Higgs production and decay: analytic results at next-to-leading order QCD", *JHEP* **12** (2005) 015, doi:10.1088/1126-6708/2005/12/015, arXiv:hep-ph/0509189.

[176] R. V. Harlander and W. B. Kilgore, "Next-to-next-to-leading order Higgs production at hadron colliders", *Phys. Rev. Lett.* **88** (2002) 201801, doi:10.1103/PhysRevLett.88.201801, arXiv:hep-ph/0201206.

[177] C. Anastasiou and K. Melnikov, "Higgs boson production at hadron colliders in NNLO QCD", *Nucl. Phys. B* **646** (2002) 220, doi:10.1016/S0550-3213(02)00837-4, arXiv:hep-ph/0207004.

[178] V. Ravindran, J. Smith, and W. L. van Neerven, "NNLO corrections to the total cross-section for Higgs boson production in hadron-hadron collisions", *Nucl. Phys. B* **665** (2003) 325, doi:10.1016/S0550-3213(03)00457-7, arXiv:hep-ph/0302135.

[179] R. V. Harlander and W. B. Kilgore, "Production of a pseudo-scalar Higgs boson at hadron colliders at next-to-next-to leading order", *JHEP* **10** (2002) 017, doi:10.1088/1126-6708/2002/10/017, arXiv:hep-ph/0208096.

[180] C. Anastasiou and K. Melnikov, "Pseudoscalar Higgs boson production at hadron colliders in next-to-next-to-leading order QCD", *Phys. Rev. D* **67** (2003) 037501, doi:10.1103/PhysRevD.67.037501, arXiv:hep-ph/0208115.

[181] C. Anastasiou et al., "Higgs boson gluon-fusion production beyond threshold in N^3LO QCD", *JHEP* **03** (2015) 091, doi:10.1007/JHEP03(2015)091, arXiv:1411.3584.

[182] C. Anastasiou et al., "Soft expansion of double-real-virtual corrections to Higgs production at $\mathrm{N^3LO}$", *JHEP* **08** (2015) 051, doi:10.1007/JHEP08(2015)051, arXiv:1505.04110.

[183] C. Anastasiou et al., "High precision determination of the gluon fusion Higgs boson cross-section at the LHC", *JHEP* **05** (2016) 058, doi:10.1007/JHEP05(2016)058, arXiv:1602.00695.

[184] U. Aglietti, R. Bonciani, G. Degrassi, and A. Vicini, "Two-loop light fermion contribution to Higgs production and decays", *Phys. Lett. B* **595** (2004) 432, doi:10.1016/j.physletb.2004.06.063, arXiv:hep-ph/0404071.

[185] R. Bonciani, G. Degrassi, and A. Vicini, “On the generalized harmonic polylogarithms of one complex variable”, *Comput. Phys. Commun.* **182** (2011) 1253, doi:10.1016/j.cpc.2011.02.011, arXiv:1007.1891.

[186] G. Degrassi and P. Slavich, “NLO QCD bottom corrections to Higgs boson production in the MSSM”, *JHEP* **11** (2010) 044, doi:10.1007/JHEP11(2010)044, arXiv:1007.3465.

[187] G. Degrassi, S. Di Vita, and P. Slavich, “NLO QCD corrections to pseudoscalar Higgs production in the MSSM”, *JHEP* **08** (2011) 128, doi:10.1007/JHEP08(2011)128, arXiv:1107.0914.

[188] G. Degrassi, S. Di Vita, and P. Slavich, “On the NLO QCD corrections to the production of the heaviest neutral Higgs scalar in the MSSM”, *Eur. Phys. J. C* **72** (2012) 2032, doi:10.1140/epjc/s10052-012-2032-z, arXiv:1204.1016.

[189] L. Hofer, U. Nierste, and D. Scherer, “Resummation of tan-beta-enhanced supersymmetric loop corrections beyond the decoupling limit”, *JHEP* **10** (2009) 081, doi:10.1088/1126-6708/2009/10/081, arXiv:0907.5408.

[190] M. Bonvini, A. S. Papanastasiou, and F. J. Tackmann, “Resummation and matching of b-quark mass effects in $b\bar{b}H$ production”, *JHEP* **11** (2015) 196, doi:10.1007/JHEP11(2015)196, arXiv:1508.03288.

[191] M. Bonvini, A. S. Papanastasiou, and F. J. Tackmann, “Matched predictions for the $b\bar{b}H$ cross section at the 13 TeV LHC”, *JHEP* **10** (2016) 053, doi:10.1007/JHEP10(2016)053, arXiv:1605.01733.

[192] S. Forte, D. Napoletano, and M. Ubiali, “Higgs production in bottom-quark fusion in a matched scheme”, *Phys. Lett. B* **751** (2015) 331, doi:10.1016/j.physletb.2015.10.051, arXiv:1508.01529.

[193] S. Forte, D. Napoletano, and M. Ubiali, “Higgs production in bottom-quark fusion: matching beyond leading order”, *Phys. Lett. B* **763** (2016) 190, doi:10.1016/j.physletb.2016.10.040, arXiv:1607.00389.